JOURNAL OF GEOPHYSICAL RESEARCH, VOL. 108, NO. A2, 1074, doi:10.1029/2002JA009620, 2003

Modeling the inner plasma sheet protons and magnetic field under enhanced convection

Chih-Ping Wang and Larry R. Lyons
Department of Atmospheric Sciences, University of California, Los Angeles, California, USA

Margaret W. Chen
Space Science Applications Laboratory, The Aerospace Corporation, El Segundo, California, USA

Richard A. Wolf and Frank R. Toffoletto
Department of Physics and Astronomy, Rice University, Houston, Texas, USA

Received 30 July 2002; revised 26 September 2002; accepted 22 November 2002; published 12 February 2003.

[1] In order to understand the evolution of the protons and magnetic field in the inner plasma sheet from quiet to disturbed conditions, we incorporate a modified version of the Magnetospheric Specification Model (MSM) with a modified version of the Tsyganenko 96 (T96) magnetic field model to simulate the protons and magnetic field under an increasing convection electric field with two-dimensional (2-D) force balance maintained along the midnight meridian. The local time dependent proton differential fluxes assigned to the model boundary are a mixture of hot plasma from the mantle and cooler plasma from the low latitude boundary layer (LLBL). We previously used this model to simulate the inner plasma sheet under weak convection corresponding to a cross polar cap potential drop ($\Delta\Phi_{PC}$) equal to 26 kV and obtained 2-D quiet time equilibrium for proton and magnetic field that agrees well with observations. We start our simulation for enhanced convection with this quiet time equilibrium and time-independent boundary particle sources and increase $\Delta\Phi_{PC}$ steadily from 26 to 146 kV in 5 hours. Simulations are also run separately to steady states by keeping $\Delta\Phi_{PC}$ constant after it is increased to 98 and 146 kV. The magnitudes of proton pressure, number density, and temperature and their increase from quiet to moderate activity ($\Delta\Phi_{PC}$ = 98 kV) are consistent with most observations. Our simulation at high activity ($\Delta\Phi_{PC}$ = 146 kV) underestimates the observed pressure and temperature. This disagreement indicates possible dependence of the boundary particle sources on activity and possible effects of solar wind dynamic pressure enhancements that have not yet been included in our simulation. The simulated equatorial pressures and temperatures show stronger enhancement on the dusk side than on the dawn side as convection is increased, while density profiles show an increase on the dawn side and a decrease on the dusk side. The simulated proton flow speed at the equatorial plane increases with enhancing convection while the overall flow direction does not change significantly, a result of enhancement in both the earthward electric drift and the azimuthal diamagnetic drift. The equatorial magnetic field strength decreases more in the near-Earth plasma sheet than at larger radial distances as $\Delta\Phi_{PC}$ increases, resulting in an increasing flat radial profile with enhancing convection. The feedbacks from diamagnetic drift and magnetic fields to increasing convection are found to restrain the pressure increase. Based on the good agreement between our results and observations at moderate activity, our magnetic field indicates that the plasma and magnetic field in the plasma sheet can be in a state far from possible force balance inconsistency during periods of moderately enhanced convection. A scale analysis of our results shows that the frozen-in condition $\mathbf{E} = -\mathbf{v} \times \mathbf{B}$ is not valid in the inner plasma sheet for moderate activity. *INDEX TERMS:* 2764 Magnetospheric Physics: Plasma sheet; 2753 Magnetospheric Physics: Numerical modeling; 2760 Magnetospheric Physics: Plasma convection; 2740 Magnetospheric Physics: Magnetospheric configuration and dynamics; 2731 Magnetospheric Physics: Magnetosphere—outer; *KEYWORDS:* magnetic field, proton pressure, proton temperature, proton density

0148-0227/03/2002JA009620$09.00

Citation: Wang, C.-P., L. R. Lyons, M. W. Chen, R. A. Wolf, and F. R. Toffoletto, Modeling the inner plasma sheet protons and magnetic field under enhanced convection, *J. Geophys. Res.*, *108*(A2), 1074, doi:10.1029/2002JA009620, 2003.

1. Introduction

[2] The convection electric field resulting from the coupling of the Earth's magnetosphere with the solar wind drives plasma in the tail plasma sheet earthward. This transport results in plasma heating and magnetic field stretching, which becomes very significant in the inner plasma sheet. (The inner plasma sheet is usually referred to the region of the plasma sheet between the earthward edge of the plasma sheet and $X_{GSM} \sim -20\ R_E$. The earthward edge of the plasma sheet is located at $X_{GSM} \sim -10\ R_E$ at midnight during quiet times. Its location moves earthward as activity increases and can move to $X_{GSM} > -5\ R_E$ during storm times.) Therefore, the inner plasma sheet plays an important role in storing energy from the solar wind. The stored energy and the transport itself are important sources for geomagnetic disturbances. For example, the spatial distribution of enhanced plasma energy is important for understanding current-wedge formation and auroral breakup during substorms [e.g., *Samson et al.*, 1992], and the inward motion of the plasma sheet during storms is important for the formation of the storm time ring current [e.g., *Chen et al.*, 1994; *Kozyra et al.*, 1998]. However, satellite measurements in this region are too scarce to depict detailed two-dimensional (2-D) distributions of particle energy spectra and bulk parameters, to reveal their variations with activity, or to realistically discern the magnetic field configuration and evolution in association with variations in activity. The limitations of available data have also hindered our ability to realistically model the inner plasma sheet and its variations with geomagnetic activity. Therefore, simulating the evolution of plasma and magnetic field in the inner plasma sheet under enhanced convection is crucial to the understanding of the role of the plasma sheet in storms and geomagnetic disturbances.

[3] The large-scale plasma transport results from electric drift and magnetic drift. The flow during quiet times is slow (~50 km/s) [*Huang and Frank*, 1986], and its velocity increases with activity [*Zhu*, 1993]. Fast earthward bursty flows (>400 km/s) are also observed in the plasma sheet [e.g., *Baumjohann et al.*, 1989; *Angelopoulos et al.*, 1993], but are confined to narrow channels of a width of a few R_E [*Sergeev et al.*, 1996; *Angelopolous et al.*, 1996]. It has been questioned if large-scale plasma flow within the inner plasma sheet could remain steady under conditions of enhanced convection. *Erickson and Wolf* [1980] suggested that steady plasma transport could result in pressures in the inner plasma sheet that would be too high to be balanced by the magnetic force, resulting in force imbalance that would disrupt the plasma transport and prevent a steady state equilibrium from being possible. This is known as pressure balance inconsistency. However, observations during steady magnetospheric convection (SMC) events show that large-scale convection can remain stable for long periods of southward interplanetary magnetic field (IMF) [*Sergeev et al.*, 1994]. Observations also show the plasma sheet plasma pressure is well balanced by the lobe magnetic pressure at different distances from the Earth and for different levels of magnetic activity [*Baumjohann et al.*, 1990]. Therefore, self-consistent modeling of plasma drift and magnetic field can help determine if the plasma magnetic field state during enhanced convection can reach a stable equilibrium or is subject to a pressure balance inconsistency.

[4] There had been several modelings of the plasma sheet using ideal MHD simulations [e.g., *Ogino et al.*, 1992; *Walker et al*, 1993] or kinetic models [e.g., *Spence and Kivelson*, 1993; *Ashour-Abdalla et al.*, 1994]. Despite the advantage of self-consistently model fields and plasma in MHD simulations, the magnetic drift is not correctly included in MHD due to the use of the frozen-in condition that is not valid in the region of the inner plasma sheet [*Hori et al.*, 2000; *Wang et al.*, 2001]. In addition, MHD does not allow for the important mixing of particles from the different sources that occurs within the inner plasma sheet as a result of energy-dependent magnetic drift. On the other hand, kinetic models can accurately calculate particles' electric and magnetic drift, but kinetic simulations are currently performed under nonconsistent fields. A self-consistent modeling of electric and magnetic drift and fields has been performed by *Toffoletto et al.* [1996, 2001]. They incorporated the Rice Convection Model (RCM) (a non-MHD model) with a magnetic field relaxation technique developed by *Hesse and Birn* [1993] to simulate the magnetotail under enhanced convection. However, because of numerical limitations in their model, they were unable to determine if a steady state configuration could be obtained under conditions of steady enhanced convection. *Hau et al.* [1989] and *Hau* [1991] artificially included the effect of magnetic drift on the radial variation of $pV^{5/3}$ in their MHD model and showed that a steady state solution is possible for the inner plasma sheet under steady convection. These previous simulations have advanced our understanding of plasma sheet dynamics. However, no non-MHD simulation has yet obtained a self-consistent magnetic field plasma pressure solution for the inner plasma sheet that remains stable under conditions of enhanced convection.

[5] Previously we self-consistently modeled protons' electric and magnetic drift under a quiet time convection electric field using a modified version of Magnetospheric Specification Model (MSM) [*Freeman et al.*, 1993] and a modified version of the Tsyganenko 96 (T96) magnetic field model [*Tsyganenko*, 1995, 1996] with force balance maintained along the midnight meridian [*Wang et al.*, 2001, 2002]. The boundary particle distributions provide particle sources for the plasma sheet population and are taken to be a mixture of particles that come from the mantle and are energized in the distant plasma sheet and that come from the low latitude boundary layer (LLBL). The boundary conditions were constructed based on Geotail observations [*Paterson et al.*, 1998] and results of the finite tail width convection model [*Spence and Kivelson*, 1993]. The results reproduced quantitatively the general features of quiet time plasma distributions and flows within the inner plasma sheet observed by different satellites.

[6] In the present work, we extend our previous quiet simulations to simulate the transport of plasma sheet pro-

tons under enhanced convection by increasing the convection electric field slowly and steadily with magnetic fields adjusted to maintain 2-D force balance along the midnight plane. The objective of this simulation are to describe the evolution of plasma and magnetic fields in the inner plasma sheet as energy input from the solar wind is increased, to account for the observed changes in the plasma sheet, to determine whether the force balance inconsistency within the inner plasma sheet can be resolved, and to investigate the processes involved in this resolution.

2. Modeling and Simulation Description

[7] In this simulation, only protons are modeled. Electrons are neglected since their pressure is typically an order of magnitude lower than the proton pressure [*Spence et al.*, 1989]. Other ion species are also neglected because of their low concentration compared to protons. Even though O^+ ions are very important for the storm time ring current, their access to the plasma sheet as a function of local time and radial distance is still not well understood. Therefore, we do not explore the O^+ contribution in this simulation. We simulate the plasma transport and energization by large-scale plasma drift; transports associated with bursty flows and substorm injection are not included. The transport of protons in the plasma sheet is modeled by a modified version of the MSM [*Freeman et al.*, 1993] under a specified electric field and a force-balanced magnetic field provided by a modified version of the T96 magnetic field model [*Tsyganenko*, 1995, 1996]. In this section, we briefly describe the models and the conditions used in this simulation of enhanced convection.

2.1. Magnetospheric Specification Model

[8] The MSM calculates the bounce-averaged electric drift and magnetic drift of a flux tube filled with an isotropic distribution of ions or electrons with a set of specified kinetic energies within the closed field line region of the magnetosphere. Assuming that the particle distributions are isotropic and that the drift motion is adiabatic, the change in the particle kinetic energy can be determined from the change of flux tube volume along its drift path according to the relation [*Wolf*, 1983]

$$E_k = \lambda V^{-2/3} \tag{1}$$

where E_k is the particle's kinetic energy, λ is constant along a particle's drift path and is called the energy invariant, and V is the flux tube volume per unit magnetic flux that is defined as $V = \int ds/B$, where B is the magnitude of the magnetic field and ds is the differential unit element along the field line. The bounce-averaged drift $\mathbf{v}_D$ at position $\mathbf{x}$ and time t is independent of pitch angle and can be described as [*Wolf*, 1983]

$$\mathbf{v}_D(\mathbf{x},t) = \frac{\mathbf{B}(\mathbf{x},t) \times \nabla\left(\Phi(\mathbf{x},t) + \lambda \mathbf{V}(\mathbf{x},t)^{-2/3}/q\right)}{|\mathbf{B}(\mathbf{x},t)|^2}, \tag{2}$$

where Φ is the electric potential, $\mathbf{B}$ is the magnetic field, and q is the particle's electric charge. The first term on the right side of (2) is the electric drift and the second term is the magnetic drift. Using an electric and a magnetic field model to provide $\Phi(\mathbf{x}, t)$ and $V(\mathbf{x}, t)$, the drift trajectory of particles of a given energy invariant λ within a flux tube is traced using (2) in the MSM.

[9] In the plasma sheet, the timescale for proton loss by strong pitch angle diffusion is much longer than the convective timescale [*Southwood and Wolf*, 1978; *Huang et al.*, 1989]; therefore proton loss through precipitation can be neglected. It has also been pointed out that waves are not strong enough to significantly change particle energies [*Huang et al.*, 1989; *Erickson*, 1992], and proton loss due to charge exchange is small in the plasma sheet. Thus, the motion of plasma sheet protons can be regarded as adiabatic. Observations show the particle distribution in the plasma sheet can be regarded as isotropic [*Stiles et al*, 1978; *Nakamura et al.*, 1991]. Therefore, the two assumptions used to derive (2) are valid in the plasma sheet and this ensures the validity of using the MSM to simulate the motion of plasma sheet protons.

[10] With specified particle distributions assigned inside the model as an initial condition and along the model boundary as particle sources, the subsequent evolution in the particle distributions resulting from different drift of different energy protons are then calculated. Details about the region of our modified MSM and how the MSM simulates particle fluxes and distribution of plasma pressure, number density, and temperature are given by *Wang et al.* [2001].

2.2. Electric and Magnetic Field Models

[11] The MSM calculates the bounce-averaged drift velocity (2) in the ionosphere. Therefore, $\mathbf{B}(\mathbf{x}, t)$ and $\Phi(\mathbf{x}, t)$ in (2) are the Earth's dipole field and the electric potential in the ionosphere. The drift due to induction electric field is negligible in the ionosphere; however, the effects of electric fields induced in the magnetosphere as the magnetic field changes are included by the MSM when particle distributions are mapped along field lines to the equatorial plane under self-consistent magnetic field. The convection electric field used in our model is essentially that of the original MSM, which has been developed to represent a realistic convection electric field. Its strength is controlled by the cross polar cap potential drop ($\Delta\Phi_{PC}$). The modeled distribution of the electric field potential inside the polar cap is based on the Heppner and Maynard empirical model [*Heppner and Maynard*, 1987]. At low latitudes (equatorward of the auroral latitudes) the distribution is based on the RCM [*Spiro et al.*, 1988], and shielding of the convection electric field is included. At auroral latitudes, the electric potential is an analytic formula that gives conventional sunward convection and joins smoothly with the formula used at higher and lower latitudes. The electric field model is controlled by parameters that include the size of the polar cap, IMF-dependent convection pattern inside the polar cap, the $\Delta\Phi_{PC}$, the latitude of shielding layer, and the penetration electric field. Except for $\Delta\Phi_{PC}$, all these parameters are originally controlled by a model input *Kp*.

[12] A magnetic field model is used to calculate $V(\mathbf{x}, t)$ and to map plasma distributions from the ionosphere to the equatorial plane. If the model magnetic fields are self-consistent with the plasma pressure, then the distributions

mapped to the equatorial plane are results of equatorial plasma motion that includes induced electric fields. We have developed a modified version of the T96 magnetic field model that maintains 2-D force balance with simulated plasma pressure in the midnight plane. The original T96 is an empirical model that generates realistic large-scale magnetic field configurations, but its current density distributions have constraints that prevent the model from being directly used to obtain a force-balanced field. Therefore, we improved the flexibility of the T96 by adding a set of additional, adjustable small-scale circular current loops [*Tsyganenko*, 1998] to the original T96 model. Descriptions of the adjustable current loops and how they are incorporated into the original T96 are given by *Wang et al.* [2002]. With this flexibility, we adjust the amplitude and direction of the additional current loops and their associated shielding magnetic field in the modified T96 to maintain $(\mathbf{j} \times \mathbf{B})_x = (\nabla p)_x$ at the equatorial plane and $\int_0^{15R_E} (\mathbf{j} \times \mathbf{B})_z dz' = p(z = 0)$ along the midnight plane in the region of the plasma sheet. Because of large computing time associated with the use of the small-scale adjustable current loops, we adjust the currents until the maximum error in the force balance requirements is $\leq$15%.

2.3. Conditions for the Simulation of Enhanced Convection

[13] We start our simulation of enhanced convection with the previously modeled quiet time equilibrium for the protons and magnetic field [*Wang et al.*, 2001, 2002] as our initial conditions. Since our focus in the current study is understating how the drift motion and energization of the plasma sheet protons vary quantitatively with an increasing convection electric field, we single out $\Delta\Phi_{PC}$ in the MSM electric field model as the only time-dependent parameter and keep other parameters at their quiescent values (that is, corresponding to $Kp = 1$ and a convection pattern for IMF $B_y = 0$, and IMF $B_z < 0$) and independent of time. In reality, the time variation of $\Delta\Phi_{PC}$ during disturbed times can be very complicated. To simplify our simulation under enhanced convection, we start with $\Delta\Phi_{PC}$ = 26 kV (the value used for our quiet time simulations) and increase $\Delta\Phi_{PC}$ steadily at a constant rate of 0.4 kV/min (In the MSM, $\Delta\Phi_{PC}$ is specified at each time step, taken to be 30 min in this simulation, and the value of $\Delta\Phi_{PC}$ between time steps is linearly interpolated. We specify that $\Delta\Phi_{PC}$ is increased by 12 kV every 30 min). The simulation is divided into two parts based on specified variations of $\Delta\Phi_{PC}$ as shown in Figure 1. We first run the simulation until $\Delta\Phi_{PC}$ is increased to 98 kV after 180 min and then keep $\Delta\Phi_{PC}$ constant for another 2 hours. This part is to simulate the evolution of the plasma sheet from quiet time to moderate activity and to determine if a steady state can be obtained when the energy input is constant. The second part continues from the first part of the simulation at = 180 min with $\Delta\Phi_{PC}$ increasing steadily after that time until it reaches 146 kV at t = 300 min. The simulation then continues with constant $\Delta\Phi_{PC}$ = 146 kV for another 2 hr to determine if a steady state can be reached under higher $\Delta\Phi_{PC}$. The results from the second part represent the plasma sheet at high activity. Note that the shielding layer in the MSM electric field model for quiet time condition maps to $\sim r = 10\ R_E$ at the night side; therefore the convection electric field is confined to mainly outside of $r = 10\ R_E$ (the convection electric field drops at $r \sim 10\ R_E$ and decreases to zero at $r \sim 7\ R_E$, see the E_y component in the study of *Wang et al.* [2001, Figure 16]). This similarly prohibits the plasma sheet from penetrating earthward of $r \sim 10\ R_E$. We do not take into account the equatorward motion of the shielding layer the might be expected under increasing convection. Thus changes in the simulation results take place mainly beyond $r = 10\ R_E$.

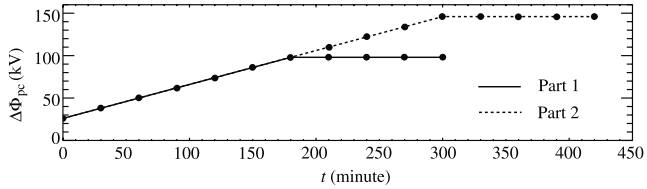

Figure 1. Assigned $\Delta\Phi_{PC}$ as a function of time. The solid line is for the simulation from quiet to moderate activity and the dotted line is for the simulation from quiet to high activity.

[14] The T96 magnetic field model is controlled by the solar wind dynamic pressure (P_{SW}), Dst, IMF B_y, and IMF B_z. The solar wind dynamic pressure determines the standoff distance and the size of the magnetopause; and the IMF and Dst determine the strengths of major magnetospheric currents (ring current, cross-tail currents, and Birkeland currents) within T96. In this simulation, we use the same values for these parameters that we used for our quiet time simulations (P_{SW} = 1 nPa, Dst = -6 nT, IMF $B_y = 0$, and IMF $B_z = -1$ nT) and keep them constant. Therefore the ring current and cross-tail current are changed only by the adjustment of the adjustable current loops that are made to maintain force balance, so that the resulting changes in magnetic field configuration are purely in response to the changes of the simulated plasma pressure.

[15] The initial proton distributions within the model region are the distributions obtained from the quiet time simulations [*Wang et al.*, 2002]. No protons of ionosphere origin are considered. The boundary particle distributions take into account warmer particles that originate from the mantle and are transported earthward from the distant tail to our model outer boundary and cooler particles from the LLBL. The mixing of these two populations is described by a bi-kappa particle distribution (a sum of two kappa distributions),

$$f = N_1 \left(\frac{m}{2\pi\kappa_1 E_{0,1}}\right)^{3/2} \frac{\Gamma(\kappa_1 + 1)}{\Gamma(\kappa_1 - 1/2)} \left[1 + \frac{E}{\kappa_1 E_{0,1}}\right]^{-\kappa_1 - 1} + N_2 \left(\frac{m}{2\pi\kappa_2 E_{0,2}}\right)^{3/2} \frac{\Gamma(\kappa_2 + 1)}{\Gamma(\kappa_2 - 1/2)} \left[1 + \frac{E}{\kappa_2 E_{0,2}}\right]^{-\kappa_2 - 1}, \quad (3)$$

where N is the densities, m is particle mass, E_0 is the energy of the peak particle flux, and κ is constant. Parameters with subscript 1 (2) determine the warmer (cooler) population. Bi-kappa distribution are assigned to the dawnside and near-Earth (inside $X_{GSM} = -10\ R_E$) duskside model boundary and single kappa distributions ($E_{0,2} = N_{0,2} = 0$) to the tail (beyond $X_{GSM} = -10\ R_E$) duskside boundary. The values of N, κ, and E vary with local time. We used observations from

Geotail [*Paterson et al.*, 1998] and the results of the finite tail width convection model [*Spence and Kivelson*, 1993] as guidelines to construct the quiet time boundary particle fluxes at different local times. The values of E's and N's for quiet time boundary conditions are given by *Wang et al.* [2001, Table 1].

[16] Initially we performed our simulations for enhanced convection using our quiet time boundary condition and kept it unchanged as we increased $\Delta\Phi_{PC}$. However, the results from this initial run showed a strong enhancement in density on the dusk side at $Y_{GSM} > 7\ R_E$, which is not seen in the DMSP observations [*Wing and Newell*, 1998]. The strong number density increase was caused by strong compression of the protons from the duskside boundary driven by their strong earthward electric drift. The disagreement suggested that the particle populations at the duskside boundary should be warmer and less dense at disturbed times than at quiet times so their duskward magnetic drift would be larger, thus reducing the number density increase. Therefore we raised the temperature and decreased the number density of the particle populations along the duskside boundary by specifying the $E_{0,1}$'s and N_1's that determine the single-kappa distributions at the duskside boundary to be the same as those that determine the first kappa distributions at the dawnside boundary. As we will show in section 3, these new boundary conditions result in better agreement between modeled and observed equatorial profiles. The modification we made to the duskside boundary condition is also consistent with our expectation for a disturbed time boundary condition based on observations and proton dynamics; this is further discussed in section 4.1. In this simulation we use this modified boundary condition and keep it independent of time in order to single out the effect of increasing convection strength on the change of the plasma sheet.

3. Simulation Results

[17] In this section, we discuss the results of the simulation for different $\Delta\Phi_{PC}$ and their comparison with observations to determine whether our calculations agree with the general observed properties of the plasma sheet. For the plasma sheet bulk parameters, qualitative descriptions of their change with activity are given in sections 3.1 to 3.3 and quantitatively comparisons with observations are investigated in section 3.4.

3.1. Proton Pressure

[18] Figure 2 shows the simulated total proton pressure in the equatorial plane near the midnight meridian for $-10\ R_E > X_{GSM} > -20\ R_E$ and for times when $\Delta\Phi_{PC}$ reached the values indicated in the figure. Individual points for this plot were obtained by averaging over bins extending 2 R_E in the X_{GSM} direction and over $|Y_{GSM}| \leq 10\ R_E$. Note that no inward motion of the inner edge of the plasma sheet from quiet to disturbed times is taken into account in this simulation. This confines the plasma sheet to mostly beyond $r = 10\ R_E$, as it was for our quiet time simulation. For all values of $\Delta\Phi_{PC}$, the proton pressure increases with decreasing distance from the Earth. The overall magnitude of the pressure increases with $\Delta\Phi_{PC}$. The pressure enhancement is larger at smaller radial distance, which is qualitatively

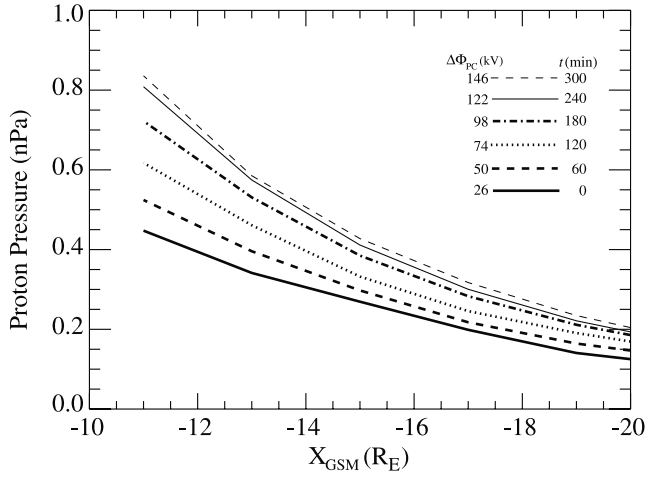

Figure 2. Equatorial proton pressure (nPa) along the midnight meridian for different $\Delta\Phi_{PC}$ from the modified MSM.

consistent with the pressure profile change from $Kp = 1$ to 3 observed by ISEE 1 [see *Spence et al.*, 1989, Figure 6].

[19] Figure 3 shows the distributions of the simulated proton pressure at the equatorial plane from low to high $\Delta\Phi_{PC}$. Proton pressures at $r < 10\ R_E$ are not shown in Figure 3 because the model convection electric field in this simulation is strongly shielded inside $r \sim 10\ R_E$, therefore, the pressures inside $r = 10\ R_E$ are mainly determined by the initial particle distributions and change only slightly with $\Delta\Phi_{PC}$. Similarly, the proton densities and temperatures at $r < 10\ R_E$ are not shown in Figures 5 and 7, respectively. For $\Delta\Phi_{PC} = 26$ kV, the pressure seen in Figure 3 is relatively uniform across the tail at larger radial distances ($X_{GSM} < -15\ R_E$) but there is a weak dawn–dusk asymmetry with slightly higher pressure on the dusk side at smaller radial distances. This asymmetry results from the duskward drift motion of protons in the plasma sheet. As $\Delta\Phi_{PC}$ increases, the pressure at larger radial distances increases mainly on the dusk side. As the radial distance decreases, pressure is seen to increase with activity on both dusk and dawn side and the dawn–dusk asymmetry becomes weaker. This can be seen in Figure 3 by the contours becoming increasingly circular as $\Delta\Phi_{PC}$ increases. To show the change of the asymmetry quantitatively, we averaged the pressure over the region $12.5\ R_E < r < 15\ R_E$ and $0 \geq X_{GSM} \geq -10\ R_E$ in the dusk to midnight quadrant and divided it by the averaged pressure over the same spatial range in the midnight to dawn quadrant. We find that the ratio is 2.33 for $\Delta\Phi_{PC} = 26$ kV and that it drops to 2.07 for $\Delta\Phi_{PC} = 98$ kV and 1.95 for $\Delta\Phi_{PC} = 144$ kV. Near the inner edge of the plasma sheet ($r \sim 10\ R_E$), the pressure enhancement on the dusk side is much stronger than the enhancement on the dawn side, resulting in a stronger dawn–dusk asymmetry at small radial distances for higher activity level (the ratio of the averaged pressure in the regions $10\ R_E < r < 11\ R_E$ and $0 \geq X_{GSM} \geq -10\ R_E$ in the dusk to midnight quadrant to the pressure in the midnight to dawn quadrant is 1.36 for $\Delta\Phi_{PC} = 26$ kV and increases to 1.48 for $\Delta\Phi_{PC} = 98$ kV and 1.51 for $\Delta\Phi_{PC} = 144$ kV). The pressure enhancement at the dawn side inner plasma sheet results primarily from the high energy protons

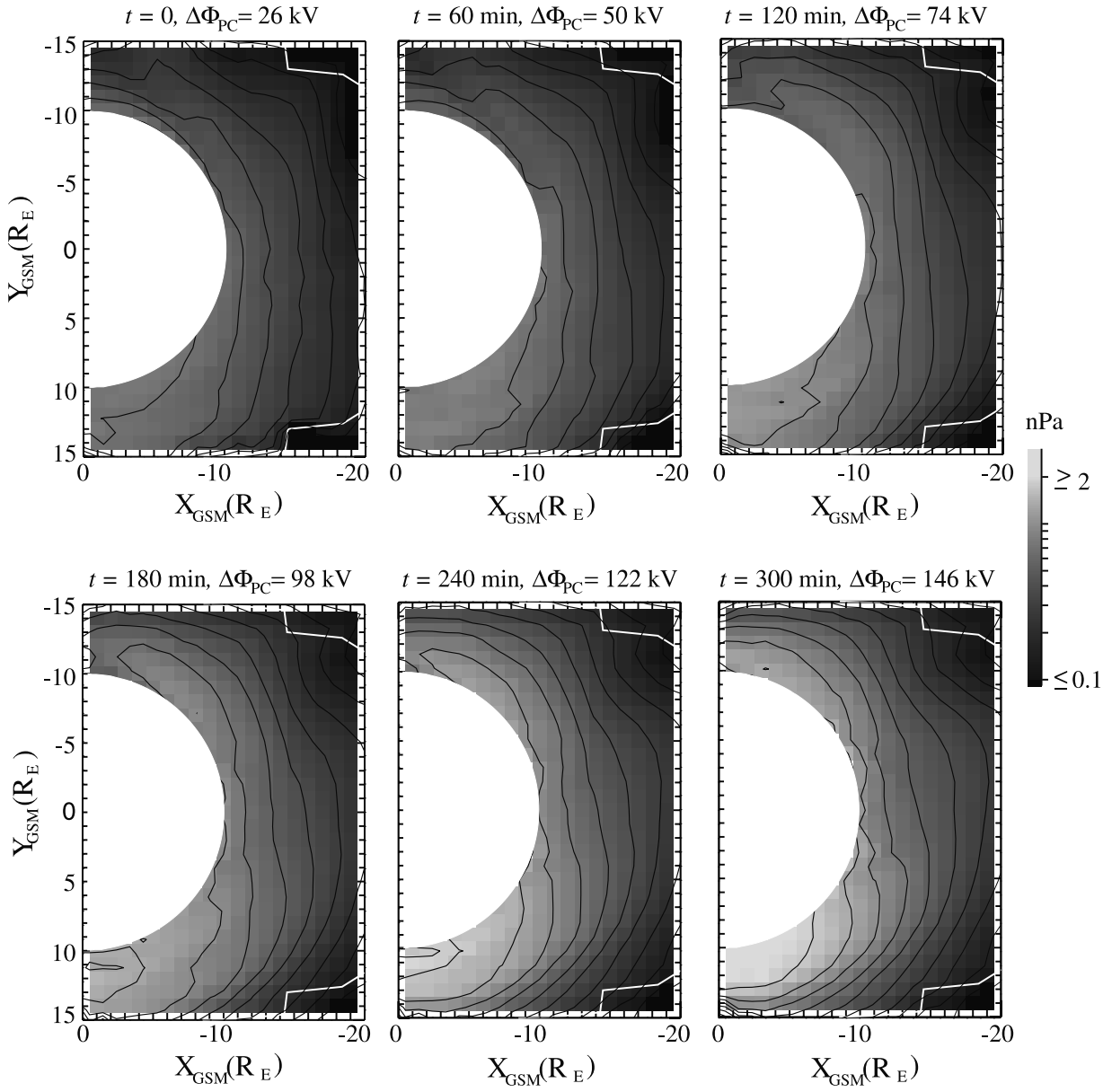

Figure 3. Proton pressure (nPa) at the equatorial plane for different $\Delta\Phi_{PC}$ from the modified MSM. The two white lines near the dawn and dusk flanks are model boundary.

from the dawn side model boundary. The increasing convection electric field allows these protons to penetrate to smaller radial distances on the dawn side before magnetic drift carries them to the dusk side. This will be discussed in section 4.2.

[20] In general, the trends of the simulated 2-D pressure distributions with increasing $\Delta\Phi_{PC}$ agree well with the trends seen in the DMSP observations from quiet to high activity levels [see *Wing and Newell*, 1998, Plate 1]. DMSP measures the plasma sheet plasma at the low altitude end of magnetic flux tubes rather than at the equatorial plane; however, *Wing and Newell* [1998] mapped the DMSP observations by assuming an isotropic distribution to show how plasma bulk parameters are distributed at the equatorial plane and how their distributions vary with geomagnetic activity. This information is not available from any other study. The DMSP pressures distributions show that the dawn–dusk asymmetry seen within $r < 15\ R_E$ at low activity weakens for moderate and high activity due to an increase of pressure on the dawn side. At the inner edge of the plasma sheet, a region of higher pressure is seen to develop in the premidnight sector at moderate activity and in both the premidnight and postmidnight sectors for high activity. These trends in the DMSP pressure distributions from quiet to high activity are reproduced by our simulations. The regions of strong pressure increase appear at smaller radial distance ($r \sim 7\ R_E$ for high activity) in the DMSP distribution than in our distribution because we did not simulate the inward motion of the plasma sheet. However, the DMSP observations show that at large radial distances ($r > 15\ R_E$) the pressure on the dawn side exceeds the pressure on the dusk side for high activity, which is not

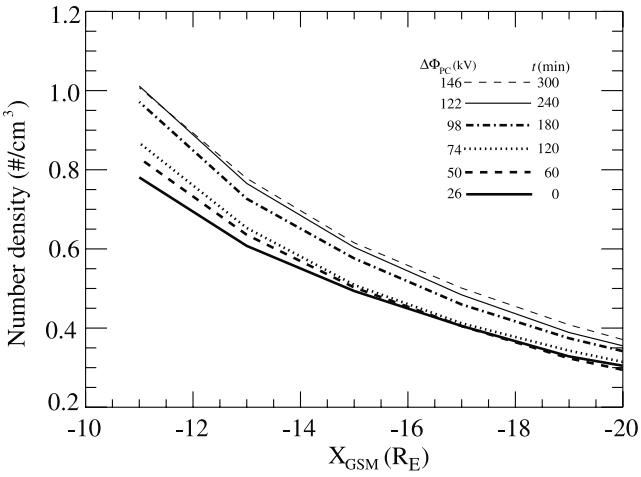

Figure 4. Equatorial proton number density (number/cm^3) along the midnight meridian for different $\Delta\Phi_{PC}$ from the modified MSM.

seen in our results. This disagreement indicates that our constant boundary condition may not be fully appropriate for high activity.

3.2. Proton Number Density

[21] Figure 4 shows the radial profiles of the simulated number density in the equatorial plane around the midnight meridian, which is averaged in the same manner as the simulated pressure shown in Figure 2. The profiles show that the number densities, for all $\Delta\Phi_{PC}$, increase with decreasing radial distance from the Earth. The overall magnitude of density becomes higher as $\Delta\Phi_{PC}$ increases but the increase is not strongly dependent on radial distance. These features of the number density profile change from quiet to high activity levels are consistent with those seen in the DMSP radial profiles [see *Wing and Newell*, 1998, Figures 7a, 7c, and 7d].

[22] The simulated proton densities within the equatorial plane for different $\Delta\Phi_{PC}$ are shown in Figure 5. For $\Delta\Phi_{PC}$ = 26 kV, we see lower density around midnight and higher density toward the dawn and dusk flanks. As $\Delta\Phi_{PC}$ increases, the number density on the dawn side is enhanced while the number density on the dusk side decreases. The dawnside enhancement is due to cooler protons being transported from the dawnside boundary. The stronger electric drift associated with higher $\Delta\Phi_{PC}$ moves particles to regions closer to the Earth, and thus to a smaller flux tube volume. Since the number of source protons along the dawnside boundary is not changed with $\Delta\Phi_{PC}$, stronger compression of the same amount of source protons results in larger density for higher $\Delta\Phi_{PC}$. The decrease on the dusk side from the quiet time density is mainly due to the change in the duskside boundary source. As mentioned in section 2.3, we raised the bulk temperature and decreased the total number density for the proton populations along the duskside boundary from their quiet time values. The increased temperature increases the duskward magnetic drift of these source particles, which restrains their earthward motion to the inner plasma sheet. This together with the decrease in the number of source particles contributes to the decrease of number density on the dusk side inner plasma sheet with increasing $\Delta\Phi_{PC}$.

[23] Our quiet time density distribution agrees well with the DMSP observations [see *Wing and Newell*, 1998, Plate 3]. From quiet to moderate activity, the DMSP density distributions show a noticeable increase in the midnight to dawn quadrant while the region of higher number density on the dusk side retreats toward the dusk flank. As a result, the dawn–dusk asymmetry with higher density on the dawn side becomes stronger at moderate activity. From moderate to high activity, the DMSP density distributions show that the asymmetric pattern remains while the overall density increases with the exception that the number density along the dusk flank is decreased. Our density changes are qualitatively consistent with the DMSP observations. Note that this good agreement could not be achieved if we did not modify our duskside boundary condition from its quiet time values. This is discussed more in section 4.1.

3.3. Proton Temperature

[24] Figure 6 shows the simulated temperature profiles in the equatorial plane around the midnight meridian, which are averaged in the same manner as the simulated pressures shown in Figure 2. The profiles show that temperature, for all $\Delta\Phi_{PC}$, increases with decreasing radial distance from the Earth. The overall magnitude of temperature increases with activity but the increase becomes small when $\Delta\Phi_{PC} > 62$ kV. This is because the temperature increase for $\Delta\Phi_{PC} > 62$ kV occurs mainly at $Y_{GSM} > 10\ R_E$ and Figure 6 only shows temperature at $|Y_{GSM}| \leq 10\ R_E$. The temperature increase does not depend strongly on radial distance. The changes of the profiles from low to moderate values of $\Delta\Phi_{PC}$ qualitatively agree with the changes in the DMSP observations from low to moderate activity levels [see *Wing and Newell*, 1998, Figures 6a, 6c, and 6d], but the increases for large values of $\Delta\Phi_{PC}$ are below those observed.

[25] Simulated proton temperatures throughout the equatorial plane for all $\Delta\Phi_{PC}$ are shown in Figure 7. The quiet time distribution ($\Delta\Phi_{PC}$ =26 kV) in Figure 7 shows that at larger radial distances the temperature is highest around midnight and with decreasing radial distance the temperature maximum moves toward dusk. This agrees well with the quiet time DMSP temperature distribution [see *Wing and Newell*, 1998, Plate 3]. As activity increases, our distributions show that the temperature peak at larger radial distances moves from midnight to positive Y_{GSM} and that there is a strong temperature increase in the midnight-to-dusk quadrant at smaller radial distances. The region of strong enhancement moves further toward dusk as $\Delta\Phi_{PC}$ increases. There is an enhancement in the midnight to dawn quadrant as well and this region of enhancement moves toward dawn with increasing $\Delta\Phi_{PC}$. The temperature does not increase much inside $|Y_{GSM}| < 10\ R_E$ for large $\Delta\Phi_{PC}$ because the regions of primary enhancement move to larger *Y*. The enhancement on the dusk side is a result of protons' duskward drift and the enhancement on the dawn side is due to the change in the trajectories of high energy particles from the dawnside boundary. The enhancement on the dawn side is not as strong as that on the dusk side, therefore there is still a dawn–dusk asymmetry with higher temperature on the dusk side for higher $\Delta\Phi_{PC}$. The changes in the regions

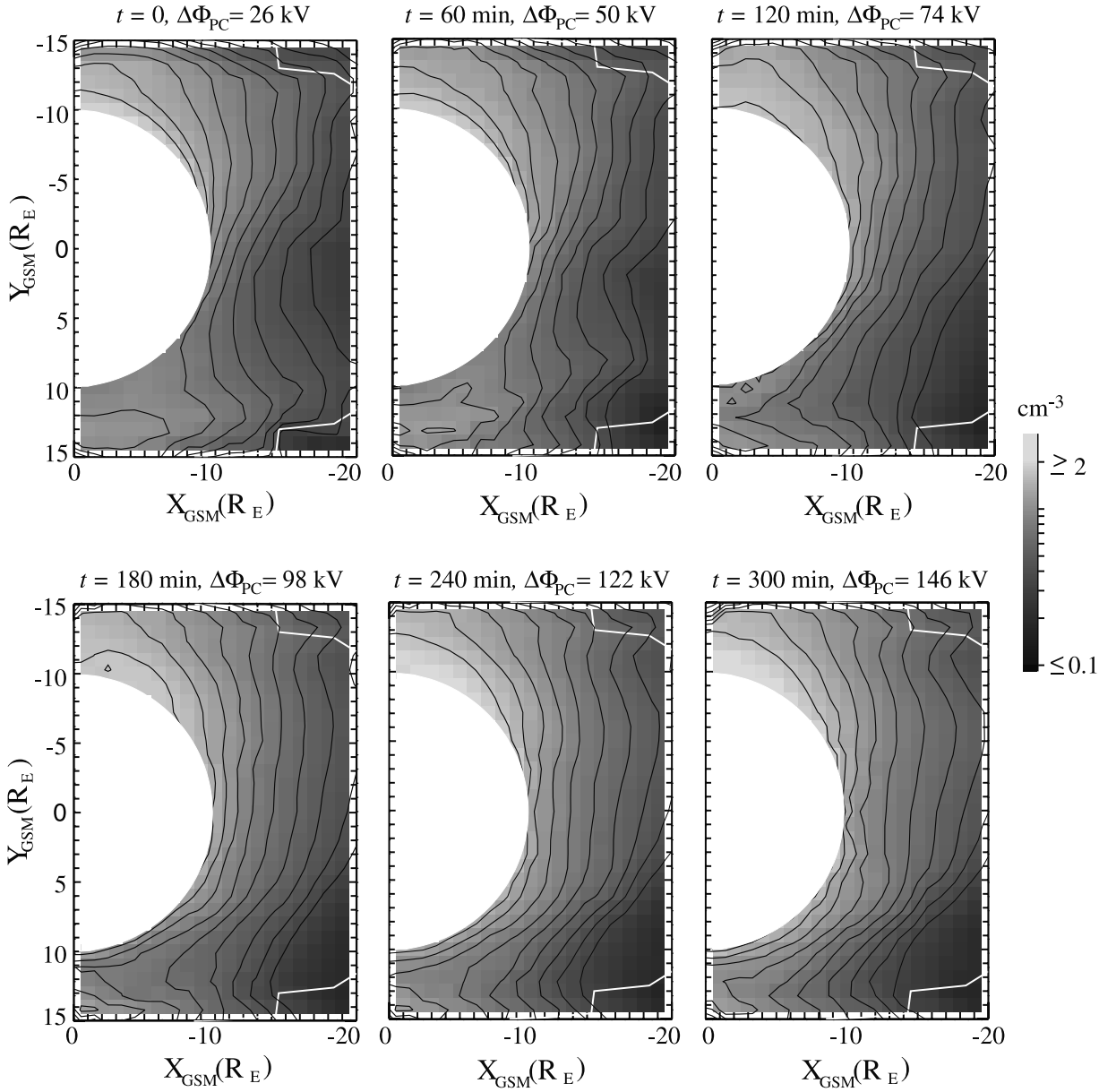

Figure 5. Proton number density (number/cm^3) at the equatorial plane for different $\Delta\Phi_{PC}$ from the modified MSM. The white lines are model boundary.

of enhancements and dawn–dusk asymmetry seen in our temperature distributions from low to high $\Delta\Phi_{PC}$ are qualitatively in agreement with the changes seen in the DMSP observations from quiet to high activity.

3.4. Dependence of Plasma Bulk Parameters on $\Delta\Phi_{PC}$

[26] Figure 8 shows how the magnitude of pressure, number density, and temperature inside $|Y_{GSM}| = 10\ R_E$ change as $\Delta\Phi_{PC}$ increases within three different X_{GSM} ranges. It is clearly seen that pressure and number density increase approximately linearly with $\Delta\Phi_{PC}$ as $\Delta\Phi_{PC}$ is increased from 26 to 110 kV and that the rate of increase becomes smaller for $\Delta\Phi_{PC} > 110$ kV. The temperature increases linearly from $\Delta\Phi_{PC} = 26$ to 62 kV and the rate of increase becomes very small for $\Delta\Phi_{PC} > 62$ kV because the temperature is enhanced mainly outside $|Y_{GSM}| > 10\ R_E$ for $\Delta\Phi_{PC} > 62$ kV. (The dashed-and-dotted line in Figure 8b is the temperature averaged over $-10\ R_E > X_{GSM} > -16\ R_E$ and $|Y_{GSM}| < 15\ R_E$ and shows a slightly higher increase rate for high $\Delta\Phi_{PC}$.) The pressure increase is seen to be stronger at smaller radial distances but the density and temperature increase rates are similar at different radial distances.

[27] In Table 1, we give the average values of proton pressure, number density, and temperature from our simulations for three different activity levels. We choose the results at $t = 0$ and $\Delta\Phi_{PC} = 26$ kV to represent the quiet time plasma sheet, results at $t = 120$ min and $\Delta\Phi_{PC} = 98$ kV to represent moderate activity, and results at $t = 180$ min and $\Delta\Phi_{PC} = 146$ kV to represent the plasma sheet at high activity. For comparison with our simulation results, we also give in Table 1 the values of plasma pressure, number

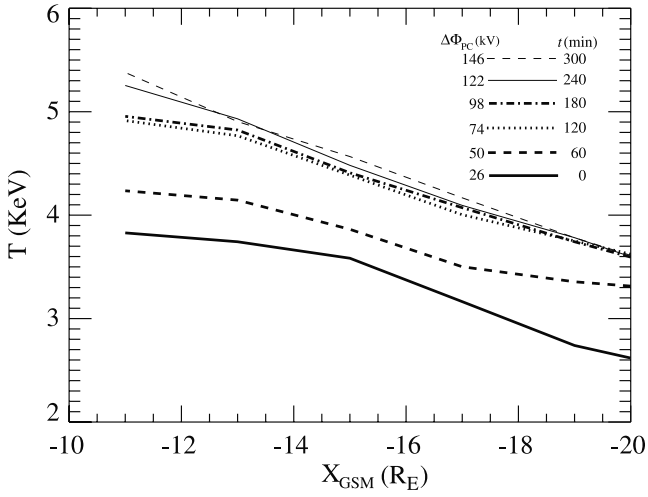

Figure 6. Equatorial proton temperature (keV) along the midnight meridian for different $\Delta\Phi_{PC}$ from the modified MSM.

density, and temperature reported from different observational studies [*Wing and Newell*, 1998; *Borovsky et al.*, 1998; *Baumjohann et al.*, 1989, 1990; *Huang and Frank*, 1994]. The regions over which the observations were averaged vary in these studies. We choose to give the values for our model as averages over the region $|Y_{GSM}| \leq 10\ R_E$ and $-10\ R_E > X_{GSM} > -22\ R_E$, which is consistent with most of the studies. The indices used by these studies to represent activity level are also different. In order to make comparisons with our results under similar magnetic activity levels, we use $\Delta\Phi_{PC} = 31.65 + 12.5(AE/100)$ [*Uvarov et al*, 1989] and $\Delta\Phi_{PC} = 16.5$ kV + 15.5 kV $\cdot$ *Kp* [*Boyle et al.*, 1997] to find the values for AE and *Kp* that corresponds to $\Delta\Phi_{PC} = 26$, 98, and 146 kV. If there is no observation corresponding to any of these AE and *Kp* values, then we use the one that is the closest. We can not find a published relationship between the b2i index used by *Wing and Newell* [1998] and $\Delta\Phi_{PC}$, so we simply choose the lowest, the highest, and the middle values of b2i in their results to be representative of our three activity levels. Nevertheless, we acknowledge that there is ambiguity in equating these indices to $\Delta\Phi_{PC}$ because $\Delta\Phi_{PC}$ acts as a driver, while these indices are a measure of the magnetosphere's response to the driver. We obtained most of the observed values in Table 1 by estimating them visually from the figures in these studies. The pressures from the study of *Huang and Frank* [1994] were calculated using their number densities and temperatures. For the results from the study of *Borovsky et al.* [1998], we use the values located on the lines they linearly fitted to their data. For the density and temperature from the study of *Wing and Newell* [1998], we took the values between $-10\ R_E > X_{GSM} > -22\ R_E$ from their radial profiles and performed the averages.

[28] From Table 1, it can be seen that for the same activity level there is a range of values from different studies. Comparisons with the observations show that our pressure, number density, and temperature are within the observed ranges for quiet and moderate activity. For high activity, our pressure is lower than all observations by a factor $\sim$2 (note that the pressure from the study of *Borovsky et al.* [1998] is for a region of larger radial distances and the pressure from the study of *Huang and Frank* [1994] is averaged over a larger Y_{GSM} range than the ranges in other studies) and our temperatures at high activity are slightly higher than the temperature in the study of *Wing and Newell* [1998] but are lower than the other observations.

[29] Our density at high activity is slightly higher than most of the observations but smaller than the observed value of *Wing and Newell* [1998]. The number densities from the study of *Wing and Newell* [1998] are higher than other observations for all activity levels. This difference may reflect two important factors that affect the observed plasma sheet number density. The first is the solar wind number density. The solar wind density within the time period of the measurement from the study of *Wing and Newell* [1998] is higher than the periods of other observations [*Richardson et al.*, 1996] and there is a strong correlation between solar wind density and plasma sheet density [*Borovsky et al.*, 1998]. The second factor is the contribution of the particles below a satellite's low energy cutoff. *Wing and Newell* [1998] took this factor into account by fitting their measured ion flux to distribution functions instead of merely computing moments within their detector's energy range. As can be seen from our simulation results in section 4.2, the contribution from low energy particles to number density is important and should not be overlooked.

[30] To investigate the dependence of these bulk parameters on activity, we also calculate in Table 1 the increase ratios of the three bulk parameters with increased activity ($R_1 \equiv$ (value of moderate activity)/(value of quiet activity), $R_2 \equiv$ (value of high activity)/(value of quiet activity)) from our results and the observations. All R_1 and R_2 values show that pressure increases with activity. However, there is uncertainty in the dependence of number density on magnetic activity from the observations. *Lannartsson* [1992] (not included in Table 1) and *Huang and Frank* [1994] found that number density decreases with increasing AE. The results from the study of *Baumjohann et al.* [1989] show that density increases with activity in the region $X_{GSM} > -14\ R_E$ but decreases with activity in the region $X_{GSM} < -14\ R_E$. On the contrary, the density increase ratios from the studies of *Wing and Newell* [1998] and *Borovsky et al.* [1998] are both larger than 1, as are our calculated increase ratios. The different dependences may result from different low energy cutoffs of the ion analyzers on the different satellites or from possible contamination by high density LLBL due to different criteria of data selection for plasma sheet encounter used in different studies [*Borovsky et al.*, 1998]. As for temperature, almost all the results show an increase with activity with the exception of the temperatures reported by *Baumjohann et al.* [1989] that decrease slightly from quiet to moderate activity in the region $X_{GSM} > -14\ R_E$.

[31] The comparisons of our increase ratios with the observations show that our pressure and temperature increases are reasonable from quiet to moderate activity, but that our simulation underestimates the pressure and temperature increase from quiet to high activity. The pressure and temperature increase ratios from quiet to high activity from the observations in Table 1 are a factor of $\sim$1.6 larger than our simulated increase ratios. (Note that the

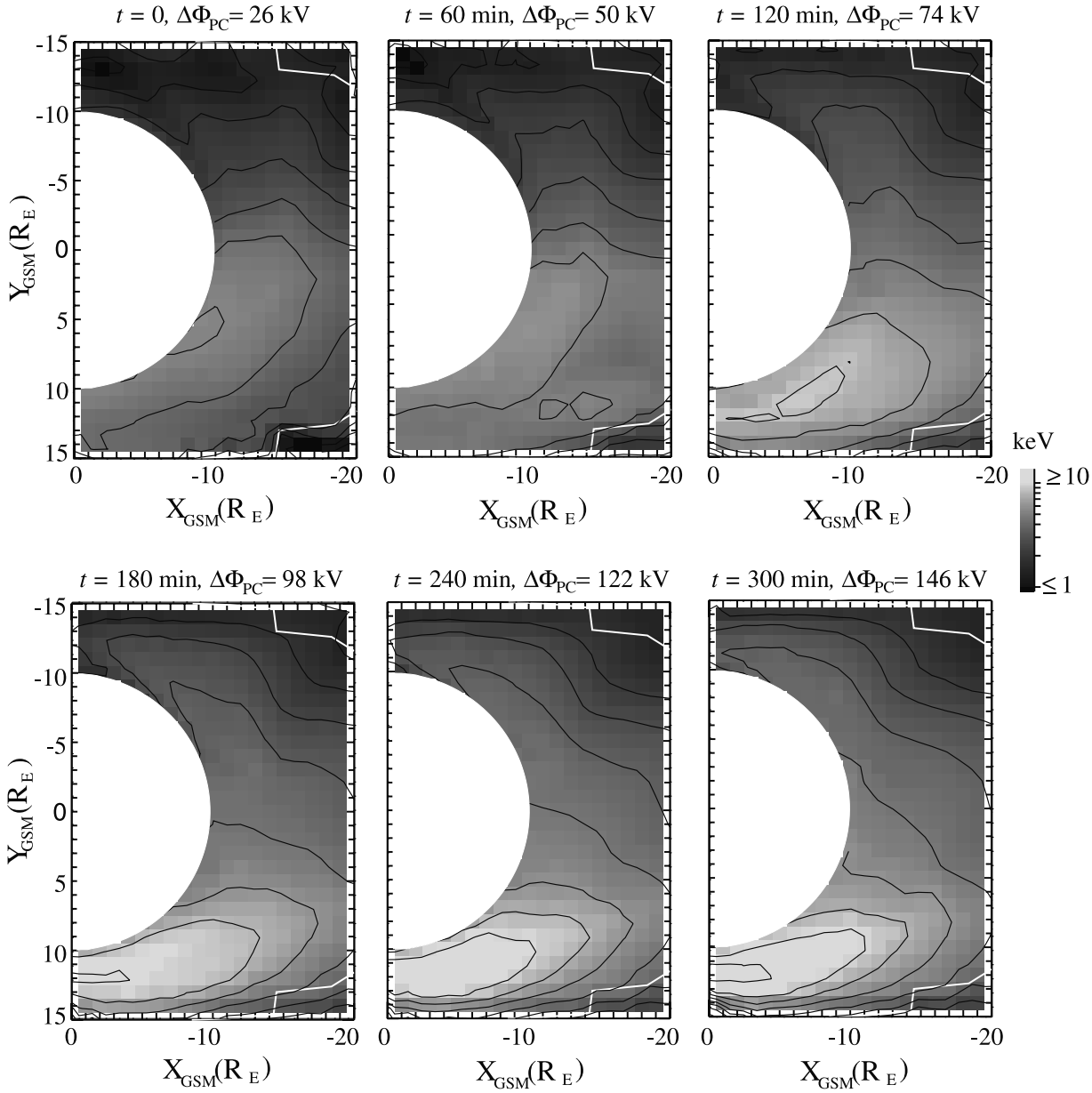

Figure 7. Proton temperature (keV) at the equatorial plane for different $\Delta\Phi_{PC}$ from the modified MSM. The white lines are model boundary.

number density from the study of *Huang and Frank* [1994] decreases with activity, which explains why their pressure increase at high activity is as small as ours.) Despite the uncertainty in density change with activity, all observations show that number density has a weak dependence on activity and this is consistent with our results.

[32] The consistency between our results and the observations of the radial profiles, the equatorial distributions, the magnitudes, and the increase ratios R_1 shows that our simulation can account for the plasma sheet evolution from quiet to moderate activity. For high activity, our radial profiles and equatorial distributions qualitatively agree with observations. The underestimate of the simulated pressure and temperature increase could be a result of the boundary conditions that we have used not being appropriate for high activity or could be the result of other factors that are not taken into account in the current simulation. This is discussed later in section 4.1.

3.5. Proton Flow

[33] The average velocity $\langle v \rangle$ of protons in a time-independent magnetic field is

$$\langle \mathbf{v} \rangle = \frac{\mathbf{B} \times \nabla \Phi}{B^2} + \frac{\mathbf{B} \times \nabla p}{neB^2}, \tag{4}$$

where n is number density and e is the electron charge. The first term on the right-hand side of (4) is the electric drift and the second term is the diamagnetic drift, which is the sum of magnetic drift and the magnetization effect.

[34] The calculated proton flows in the equatorial plane from (4) for different $\Delta\Phi_{PC}$ are shown in Figure 9. In this simulation, the magnitude of the induction electric field in

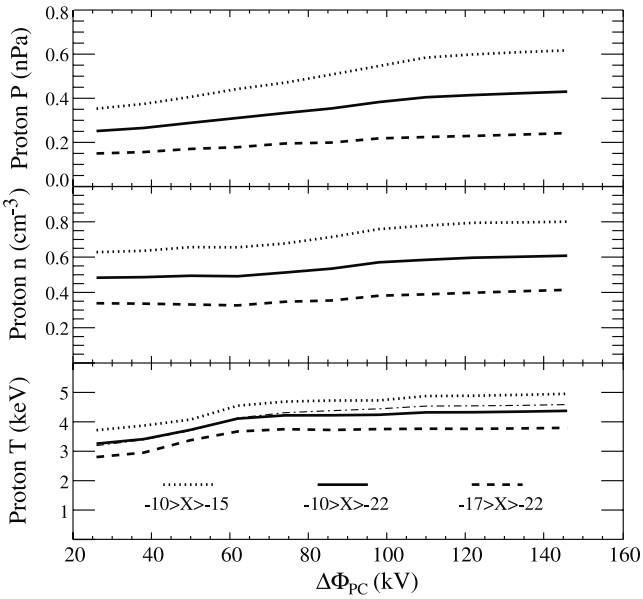

Figure 8. (a) Proton pressure (nPa), (b) proton number density (number/cm^3), and (c) proton temperature (keV) averaged over $|Y_{GSM}| \leq 10\ R_E$ as a function of $\Delta\Phi_{PC}$. Dashed lines are for the region $-10\ R_E > X_{GSM} > -16\ R_E$, dotted lines are for the region $-16\ R_E > X_{GSM} > -22\ R_E$, and solid lines are for the region $-10\ R_E > X_{GSM} > -22\ R_E$. The thin dashed-and-dotted line in proton temperature is averaged over $|Y_{GSM}| \leq 15\ R_E$ and $-10\ R_E > X_{GSM} > -22\ R_E$.

the equatorial plane is about 1/5 the magnitude of the convection electric field; thus, its effect on electric drift is neglected when using (4) to calculate $\langle \mathbf{v} \rangle$. The electric drift is mainly directed toward the Earth and its magnitude is relatively constant across the tail due to the relatively uniform duskward convection electric field across the tail generated by the MSM. The diamagnetic drift for protons is mainly directed azimuthally toward positive Y_{GSM}. For quiet times, the flow near the dawn flank of the plasma sheet is dominated by electric drift. Since protons in this region are relatively cool (see Figure 7) and their number density is relatively high (see Figure 5), their diamagnetic drift is small. Because the number density decreases and the pressure increases from the dawn flank toward midnight, the component of diamagnetic drift gradually becomes stronger from the dawn flank to midnight and eventually becomes as important as the electric drift. As a result, the flows are gradually diverted toward the dusk side as the diamagnetic drift grows. The diamagnetic drift dominates the premidnight flow. It then gradually decreases in magnitude toward the dusk flank due to the larger number density along the dusk flank and becomes smaller than the magnitude of electric drift. Therefore, this flow pattern shows that the plasma transported earthward from the distant tail is mainly diverted toward dusk in the inner plasma sheet and only plasma near the dawn flank maintains its earthward motion. The asymmetry in the flow indicates that the cool protons on the dawn side continue their motion to the dayside magnetopause but part of the hot proton population on the dusk side may be lost across the dusk magnetopause

Table 1. Comparison of Our Simulation Results With Observations

	Our Simulation	*Wing and Newell* [1998]		*Borovsky et al.* [1998]	*Baumjohann et al.* [1989, 1990]		*Huang and Frank* [1994]
Region (GSM R_E)	$\|Y\| < 10$ $-10 > X > -22$	$\|Y\| < 10$ $-11 > X > -19$		$\|Y\| < 10$ $-17.5 > X > -22.5$	$\|Y\| < 12$ $-11 > X > -19$		$\|Y\| < 20$ $-10 > X > -23$
Activity level Q: quiet M: moderate H: high	Q: $\Delta\Phi_{PC}$ = 26 kV M: $\Delta\Phi_{PC}$ = 98 kV H: $\Delta\Phi_{PC}$ = 146 kV	Q: b2i = 69 M: b2i = 65 H: b2i = 61		Q: *Kp* = 1 M: *Kp* = 5 H: *Kp* = 7	For pressure Q: AE = 125 M: AE = 550 H: AE = 875 For density and temperature Q: AE = 60 M: AE = 660		Q: AE = 50 M: AE = 550 H: AE = 950
Pressure (nPa)	Q: 0.25 M: 0.38 H: 0.43	$\|Y\| < 12$ $X > -15$ Q: 0.4 M: 0.57 H: 0.8	$\|Y\| < 12$ $X < -15$ Q: 0.28 M: 0.5 H: 0.75	Q: 0.11 M: 0.26 H: 0.41	$X > -15$ Q: 0.45 M: 0.74 H: 0.95	$X < -15$ Q: 0.35 M: 0.46 H: 1.05	Q: 0.18 M: 0.28 H: 0.3
Pressure increase ratios	*R1* = 1.52 *R2* = 1.7	*R1* = 1.43 *R2* = 2.0	*R1* = 1.78 *R2* = 2.67	*R1* = 2.36 *R2* = 3.72	*R1* = 1.64 *R2* = 2.11	*R1* = 1.31 *R2* = 3.0	*R1* = 1.55 *R2* = 1.66
Number density (cm^{-3})	Q: 0.48 M: 0.57 H: 0.61	Q: 0.84 M: 0.92 H: 1.06		Q: 0.18 M: 0.23 H: 0.26	$\|X\| < 14$ Q: 0.28 M: 0.43	$\|X\| > 14$ Q: 0.25 M: 0.13	Q: 0.38 M: 0.29 H: 0.28
Density increase ratios	*R1* = 1.17 *R2* = 1.25	*R1* = 1.09 *R2* = 1.26		*R1* = 1.27 *R2* = 1.44	*R1* = 1.53	*R1* = 0.52	*R1* = 0.76 *R2* = 0.73
Temperature (keV)	Q: 3.25 M: 4.24 H: 4.37	Q: 2.31 M: 3.31 H: 3.72		Q: 4.0 M: 7.5 H: 11.0	$\|X\| < 14$ Q: 4.55 M: 3.78	$\|X\| > 14$ Q: 3.87 M: 4.55	Q: 3 M: 5.8 H: 6.7
Temperature increase ratios	*R1* = 1.3 *R2* = 1.34	*R1* = 1.43 *R2* = 1.6		*R1* = 1.88 *R2* = 2.75	*R1* = 0.83	*R1* = 1.17	*R1* = 1.93 *R2* = 2.23

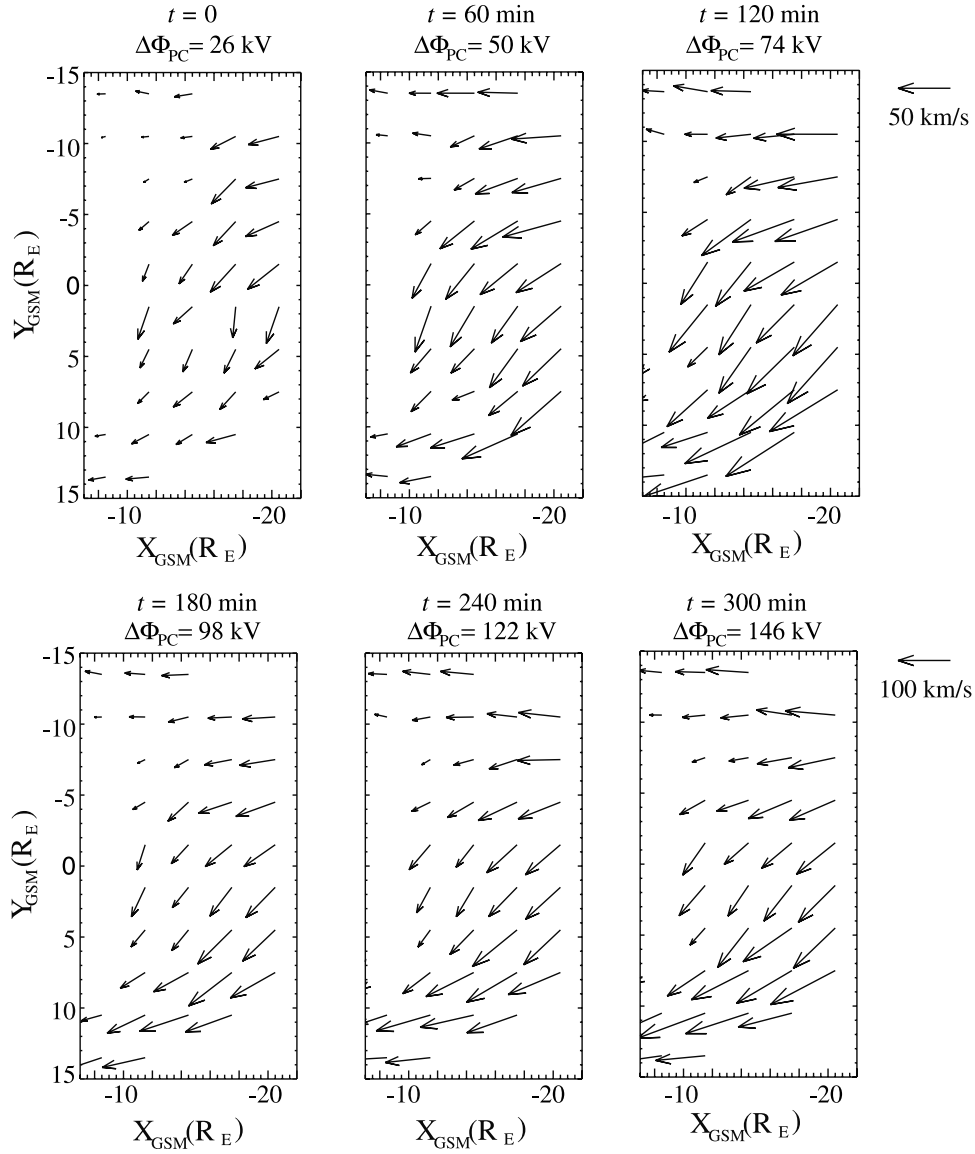

Figure 9. Proton flow in the equatorial plane for different $\Delta\Phi_{PC}$ from the modified MSM. The unit vector is 50 km/s for flows for $\Delta\Phi_{PC}$ = 26, 50, and 74 kV and is 100 km/s for flows for $\Delta\Phi_{PC}$ = 98, 122, and 146 kV.

because of azimuthal drift. The flow speed in the plasma sheet is ~10–50 km/s during quiet times. In general, the speed and pattern of our simulated flow agree well with quiet observations from AMPTE, ISEE 2 [*Angelopoulos et al.*, 1993; *Angelopoulos*, 1996] [see *Wang et al.*, 2001, Figure 11], and ISEE 1 [*Zhu*, 1993].

[35] As the $\Delta\Phi_{PC}$ increases, we can see from Figure 9 that the overall flow speed increases while the flow pattern basically remains unchanged with no significant changes in flow direction. This indicates that while the electric drift is enhanced as a result of increased convection electric field, the diamagnetic drift is enhanced as well. The averaged increase in flow speed is about a factor of 2.82 from $\Delta\Phi_{PC}$ = 26 to 98 kV and a factor of 4.04 from $\Delta\Phi_{PC}$ = 26 to 144 kV. The increase of velocity with geomagnetic activity is consistent with the ISEE 1 observations [*Zhu*, 1993], which shows the velocity during periods of AE > 100 nT is about twice the velocity during periods of AE < 100 nT. Also, the independence of the flow pattern on activity can be seen in the study of *Zhu* [1993, Figures 2 and 3]. *Hori et al.* [2000, Figure 1] show ion flow obtained from the Geotail spacecraft. Despite their flow being averaged over all activity levels, their flow pattern is very similar to our pattern, an agreement that suggests the flow direction does not change significantly with activity. The enhancement of diamagnetic drift with activity plays an important role in maintaining steady plasma transport under enhanced convection. This is discussed in section 4.5.

3.6. Magnetic Field

[36] The equatorial magnetic field strengths along the midnight meridian for different $\Delta\Phi_{PC}$ are plotted in Figure 10. In general, the field strengths, for all activity levels, decrease with increasing distance from the Earth but the radial gradient changes significantly. In the plasma sheet, the decrease of the strength with increased activity is much

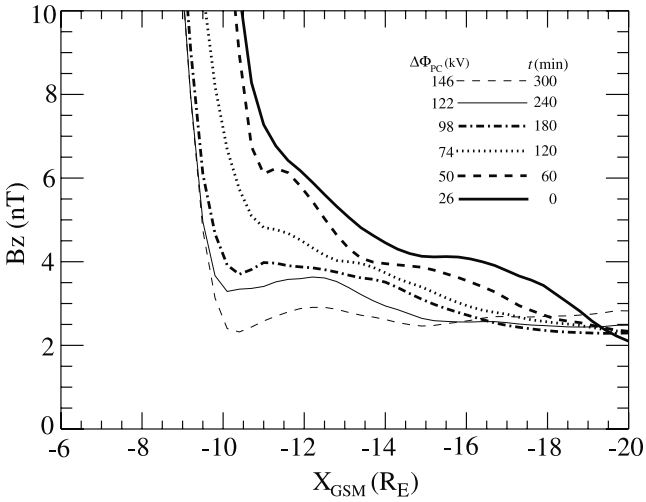

Figure 10. Equatorial magnetic field strength (nT) along the midnight meridian for different $\Delta\Phi_{PC}$.

stronger at the near-Earth edge than at larger distances. As a result, the radial profile becomes flatter as $\Delta\Phi_{PC}$ increases. The magnetic field in the inner magnetosphere remains strong; therefore a sharp radial gradient is formed at the inner edge of the plasma sheet ($\sim r$ = 10–11 R_E). The decreasing field strength with increasing $\Delta\Phi_{PC}$ in the plasma sheet is a result of field lines stretching caused by the increasing azimuthal current density carried by protons with increasing azimuthal diamagnetic drift. The significant stretching of magnetic field lines from low to high $\Delta\Phi_{PC}$ is shown in Figure 11. The radial profile for enhanced convection is qualitatively consistent with the results of *Sergeev et al.* [1994]. By using near-geostationary magnetic field observations, magnetic field modeling, and a novel diagnostic technique (isotropic boundary algorithm), *Sergeev et al.* [1994] showed evidences for field line stretching and the formation of a sharp radial gradient during SMC events.

[37] Previous plasma sheet modeling for enhanced convection [*Hau et al.*, 1989; *Erickson*, 1992; *Toffoletto et al.*, 2001] and modeling fits to observations [*Sergeev et al.*, 1994] showed that a B_z minimum is formed at the location of the sharp field gradient. As shown in Figure 10, our magnetic field profiles show that a local field minimum develops at the location of the sharp field gradient ($r \sim 10$ R_E) only for $\Delta\Phi_{PC}$ > 98 kV. (Note that the small dips right at the location of the sharp gradient seen in the profiles at $\Delta\Phi_{PC}$ = 50 and 98 kV in Figure 10 are due to a nonsmooth distribution of our small-scale adjustable current density.) In addition, the magnetic field strengths at larger distances ($r \sim 20$ R_E) are seen to increase at high $\Delta\Phi_{PC}$. The formation of the local field minimum and the field increase at larger radial distances is a result of the pressure increase at smaller radial distances being much greater than the increases at larger distances at high $\Delta\Phi_{PC}$, as seen in Figure 2. The current density change corresponding to this distance-dependent pressure increase generates a net magnetic field perturbation that is positive at larger distances. This is further discussed in section 4.5. It can be seen in Figure 10 the location of the sharp radial gradient moves slightly earthward as $\Delta\Phi_{PC}$ increases ($\sim$1 R_E from $\Delta\Phi_{PC}$ = 26 to 146 kV). This is a response to a change of the earthward edge of the Alfvén layers, which is moved slightly earthward by the increased convection electric field at the inner edge of the plasma sheet even though the shielding layer is not moved. The earthward penetration is small compared to the space between the model grid points in the equatorial plane, which are mapped from the grid points on the ionosphere. This space increases as field lines become increasingly stretched; therefore sometimes the small earthward motion cannot be resolved by our grid, as seen in the field profiles for $\Delta\Phi_{PC}$ = 122 and 146 kV in Figure 10.

[38] The change of the magnetic field configuration implies changes in the spatial distribution of magnetic flux tube volumes. Its effect on plasma energization is addressed in section 4.5.

3.7. Steady State Plasma Sheet

[39] We have run our simulation under constant $\Delta\Phi_{PC}$ after $\Delta\Phi_{PC}$ is increased to 98 kV at t = 180 min and to 146 kV at t = 300 min (see Figure 1) to see if the plasma and magnetic field can reach a steady state. In both cases, we find that pressure keeps increasing after $\Delta\Phi_{PC}$ is kept constant but that the pressure changes are relatively small. The pressure increase is seen mainly at smaller radial distances because the particles that enter from the model boundary need more time to travel to smaller radial distances. The increase gradually becomes smaller until there is no further change in the pressure (about 1 hour for $\Delta\Phi_{PC}$ = 98 kV and 0.5 hour for $\Delta\Phi_{PC}$ =146 kV) and both the pressure and magnetic field reach a steady state. Therefore, our simulation indicates that the plasma transport under constant convection can result in a steady state plasma sheet. The steady state plasma pressure and the equatorial magnetic field strength along the midnight meridian for $\Delta\Phi_{PC}$ = 98 kV are shown in Figure 12 and compared with the plasma pressure and field strength for $\Delta\Phi_{PC}$ = 98 kV at t = 180 min. The most significant difference in the magnetic field profiles is the formation of a modest field minimum at the inner edge of the plasma sheet when the plasma sheet reaches steady state. This, like the field minimum occurs at $\Delta\Phi_{PC}$ > 98 kV, is due to the pressure increasing mainly at smaller radial distances after $\Delta\Phi_{PC}$ becomes constant. The pressure at the steady state for constant $\Delta\Phi_{PC}$ = 146 kV is slightly higher than the pressure for $\Delta\Phi_{PC}$ = 146 kV at t = 300 min at smaller radial distances, but the pressure is almost the same at larger distances. Responding to this pressure increase, the field strength at the inner edge of the plasma sheet becomes smaller as the pressure approaches the steady state, resulting

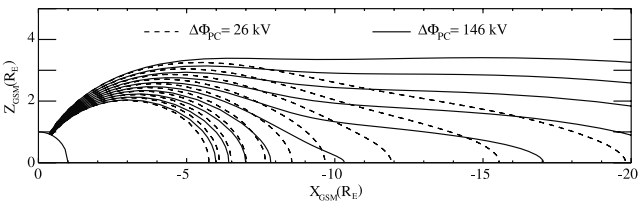

Figure 11. The magnetic field lines traced from 10 different latitudes along the midnight meridian for $\Delta\Phi_{PC}$ = 26 kV (dashed lines) and for $\Delta\Phi_{PC}$ = 146 kV (solid lines).

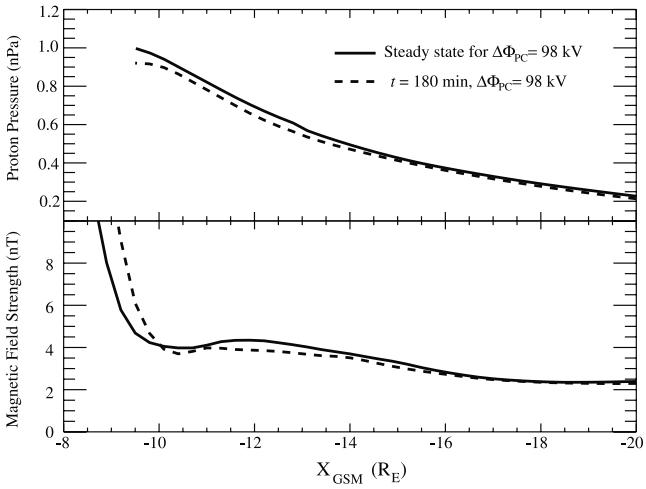

Figure 12. (a) Equatorial proton pressure (nPa) and (b) equatorial magnetic field strength along the midnight meridian at t = 180 min and $\Delta\Phi_{PC}$ = 98 kV (dashed lines) and at the steady state for constant $\Delta\Phi_{PC}$ = 98 kV (solid lines).

in a field minimum during the steady state that is slightly deeper than the field minimum at t = 300 min.

4. Additional Discussion

4.1. Model Boundary Conditions for High Activity

[40] The fact that our simulation for high $\Delta\Phi_{PC}$ underestimates the pressure and temperature in the plasma sheet for high activity indicates that the drift transport alone cannot energize plasma to the observed pressure and temperature for high geomagnetic activity. This suggests that changes in the boundary condition and other control parameters with convection strength may be important contributors to plasma sheet structure during such periods.

[41] It has been shown from observations that the LLBL is an important source for quiet time plasma sheet particles [*Fujimoto et al.*, 1998]. It is likely that quiet time conditions are favorable for processes (e.g., the Kelvin–Helmholtz instability) [*Otto and Fairfield*, 2000; *Fairfield et al.*, 2000] that allow cold magnetosheath particles to enter the magnetosphere through the flanks. However, the LLBL is much thinner during disturbed times than during quiet times [*Mitchell et al.*, 1987], which implies that the particle entry processes from the flanks may become less efficient during disturbed times [*Miura*, 1995] and therefore the particle supply to the plasma sheet from the LLBL is lower if the magnetosheath density remains the same. In addition, *Wing and Newell* [2002] show the decrease in the number density along the flanks from periods of southward IMF to northward IMF is more significant in the dusk flank. As for the particles originating from the mantle, those of higher energy that do not have access to the distant tail plasma sheet at low $\Delta\Phi_{PC}$ could enter the plasma sheet at higher $\Delta\Phi_{PC}$ because of stronger electric drift toward the equatorial plane. In addition, during the earthward transport from the distant tail plasma sheet to our model boundary, particles are energized and the energization should be stronger at higher $\Delta\Phi_{PC}$. This should affect our duskside model boundary more than the dawnside boundary because of protons' duskward drift. Combing these two effects, we expect that the number of high energy particles at the tail model boundary should be larger for disturbed times than for quiet times. Taking into account both the particles from the LLBL and distant tail, the boundary particle sources are expected to become warmer and less dense with increasing $\Delta\Phi_{PC}$ and the change of magnitude should be more significant on the duskside model boundary.

[42] In the current simulation, we modified the boundary condition from its quiet time values because of a significant qualitative disagreement in the dusk to midnight quadrant between our initial runs and the DMSP observations [*Wing and Newell*, 1998]. However, there was no significant disagreement in the midnight to dawn quadrant, which indicates that the particle distributions at the dawnside boundary do not change significantly from quiet to disturbed times. These results are qualitatively consistent with our argument described in the previous paragraph. To provide simple but appropriate boundary conditions for disturbed times, we have kept the dawnside boundary condition unchanged and decreased the number density and increased the temperature at the duskside boundary from their quiet time values. We did not make a further modification to allow the boundary conditions to change with $\Delta\Phi_{PC}$ because the primary goal of the current study is to isolate the effects of increasing values of $\Delta\Phi_{PC}$ on the plasma sheet.

[43] Another factor that could contribute significantly to the plasma pressure increase at high activity, but which we have not included in the current simulation, is enhancement in the solar wind dynamic pressure. Compression of the magnetosphere by an increase in the solar wind dynamic pressure results in an increase in the magnetic pressure of the tail lobes, and thus also of the plasma pressure at the equator. *Borovsky et al.* [1998] show there is a strong correlation between the solar wind dynamic pressure and the plasma sheet pressure. The T96 model shows that the lobe magnetic field pressure increases by a ratio that roughly equals the square root of the increase ratio of the solar wind dynamic pressure if other control parameters are kept constant (e.g., a change in the dynamic pressure from 1 to 10 nPa increases the lobe magnetic pressure by a factor of $\sim$3.3). Solar wind dynamic pressure also strongly affects ionospheric currents and auroral activity [e.g., *Shue and Kamide*, 1998; *Zesta et al.*, 2000]. Thus compression of the magnetosphere may contribute significantly to plasma pressure and temperature increases observed during periods of enhanced geomagnetic activity. In addition, if solar wind dynamic pressure enhancement is either partly or totally due to an increase in solar wind density, then the number of particles that have access to the magnetosphere would be increased. This could affect the total number of particles at our model boundary.

[44] In future we plan to examine the effect of boundary conditions changes in response to enhancements in $\Delta\Phi_{PC}$ and solar wind dynamic pressure, as well as of compression due to enhancement of the solar wind dynamic pressure, on our simulated pressures and temperatures for high activity.

4.2. Drift Paths of Low and High Energy Protons

[45] Figure 13 compares the equatorial partial drifts (computed using (4) with a partial pressure p integrated over a given energy range) of low energy protons (protons

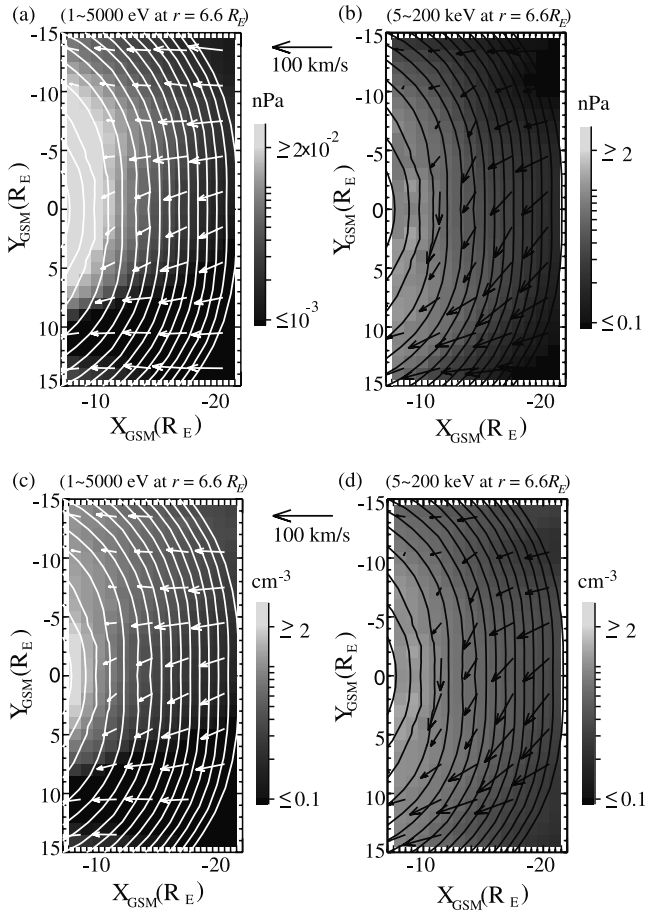

Figure 13. Equatorial proton partial pressure for (a) particles that have energies 1–5000 eV at $r = 6.6\ R_E$ and (b) particles that have energies 5–200 keV at $r = 6.6\ R_E$ (Note that the scale for pressure in (a) is 2 orders of magnitude smaller than the scale in (b)). Equatorial proton number density for (c) particles that have energies 1–5000 eV at $r = 6.6\ R_E$ and (d) particles that have energies 5–200 keV at $r = 6.6\ R_E$. The arrows are partial flow corresponding to energy range indicated. The thin lines are contours of constant flux tube volume.

having energies 1 eV to 5 keV at $r = 6.6\ R_E$) and high energy protons (5–200 keV at $r = 6.6\ R_E$) for $\Delta\Phi_{PC} = 98$ kV. Superimposed on the partial drifts is partial pressure, partial number density in the equatorial plane, and contours of constant flux tube volume. As can be seen from Figure 13, the pressure born by high energy protons is 2 orders of magnitude larger than that pressure of the low energy protons. (Note that the pressure scale for Figure 13a is 2 orders of magnitude smaller than the scale for Figure 13b.) The number densities for the higher and lower energy protons are similar. This indicates that a satellite measurement can significantly underestimate number density if the low energy cutoff for its instrument is too high; therefore it is necessary to estimate and include the contribution from particles below the cutoff when obtaining number densities, as was done by *Wing and Newell* [1998].

[46] As shown in Figure 13, the low energy protons flow mainly perpendicular to the contours of flux tube volume while the high energy protons flow at an angle off of the perpendicular direction because of their higher diamagnetic drift. The difference in the drift directions relative to the contours of constant flux tube volume shows that low energy protons will experience more flux tube volume reduction than high energy protons along their respective drift paths. Therefore, the increase ratios for density and pressure resulting from compression of the flux tube volume (nV = constant and $pV^{5/3}$ = constant) are significantly larger for low energy protons than for high energy protons. Even though the low energy protons have large pressure increase ratios, their pressure is too low to be increased to a magnitude that is comparable to the pressure of high energy particles. On the other hand, the smaller increase ratio constrains the increase in the pressure of the high energy particles.

[47] The drift paths also determine the regions in the plasma sheet that can be reached by protons of different energies. As shown in Figure 14, protons whose energy is 70 keV at $r = 6.6\ R_E$ (this particular energy channel is chosen because of its large partial pressure. It contributes ~1/3 of the total pressure near midnight) originating from the dawn side can penetrate to a smaller radial distance on the dawn side for $\Delta\Phi_{PC} = 98$ kV than for $\Delta\Phi_{PC} = 26$ kV before drifting to the dusk side. This penetration not only

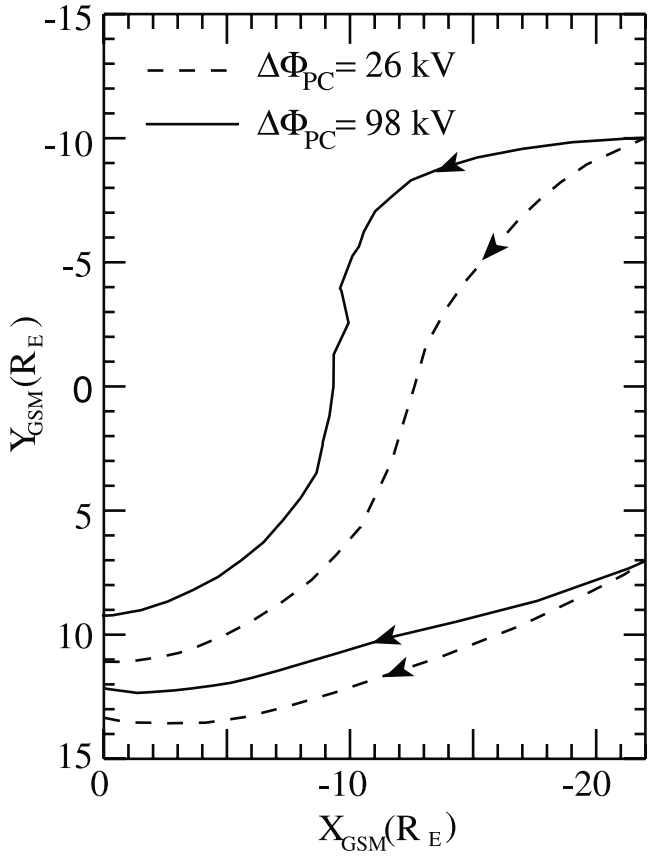

Figure 14. The drift paths for protons that have energy 70 keV at $r = 6.6\ R_E$ starting from locations $[X_{GSM},Y_{GSM}] = [-22\ R_E,-10\ R_E]$ and $[X_{GSM},Y_{GSM}] = [-22\ R_E,10\ R_E]$ for $\Delta\Phi_{PC} = 26$ kV (dashed lines) and for $\Delta\Phi_{PC} = 98$ kV (solid lines).

increases the energization, it also moves the region affected by protons of this particular energy further earthward and dawnward, which explains the pressure enhancement on the dawn side of the plasma sheet for higher activity as shown in Figure 3. On the dusk side, the drift path moves a small amount earthward with increasing $\Delta\Phi_{PC}$, which affects energy increase for the protons but does not significantly change the region to which the protons have access.

4.3. Force Balance Inconsistency

[48] The compression of plasma as it is transported earthward from a larger magnetic flux tube volume to a smaller one results in an increase of plasma pressure. If the plasma is isotropic and the compression is adiabatic, transport from the distant tail to the inner plasma sheet along the midnight meridian might give a pressure that is too high for the pressure gradient force in the inner plasma sheet to be balanced by the magnetic force. This pressure balance inconsistency was first considered by *Erickson and Wolf* [1980]. However, observations during SMC events show that large-scale convection can remain stable for several hours under southward IMF condition [*Sergeev et al.*, 1994], which indicates that the force balance can be maintained. It was suggested that the inconsistency might be resolved by taking into account the azimuthal magnetic drift [*Tsyganenko*, 1982; *Kivelson and Spence*, 1988] and a self-consistent magnetic field [*Hau et al.*, 1989; *Hau*, 1991; *Erickson*, 1992].

[49] *Hau* [1991] used a MHD model to obtain steady state solutions for the inner plasma sheet, but the effect of magnetic drift on the radial variation of $pV^{5/3}$ was artificially included and it is not certain if the possible steady states they obtained can be reached in a dynamic evolution. *Toffoletto et al.* [1996, 2001] incorporated the RCM with a magnetic field relaxation technique developed by *Hesse and Birn* [1993] to simulate the plasma sheet under enhanced convection. The RCM uses the same methods to calculate the electric and magnetic drifts as those used in the MSM, but it also models self-consistently the interaction between the plasma sheet and the ionospheric electric potential through field aligned current computed at the equatorial plane. Their results show that the plasma pressure increases and the magnetic field adjusts to maintain force balance. This force balance is maintained for at least for 100 min under steady convection corresponding to $\Delta\Phi_{PC}$ = 100 kV. However, the stretched field lines make it difficult for the RCM to calculate the field aligned current at the equatorial plane because the space between grid points becomes too large and the code eventually breaks. Because of this limitation, Toffoletto et al. were not able to obtain a steady and stable plasma sheet under steady enhanced convection.

[50] The partial pressure corresponding to particles of a given energy range varies with $V^{-5/3}$ as a flux tube is compressed or expanded. Previous modeling has suggested that, when $pV^{5/3}$ increases in the inner plasma sheet, the response of the force-balanced magnetic field is to stretch the field lines, thus increase flux tube volume and moderate the pressure. As a result, the radial profile of magnetic field strength at the equatorial plane becomes flatter and a local minimum is formed at the inner edge of the plasma sheet. Simulations also show that the local minimum is deeper if the pressure increase in the inner plasma sheet is larger [*Erickson*, 1992]. This implies that the strength at the local minimum could approach zero (formation of a neutral point near the Earth) if $pV^{5/3}$ gets very high. This also suggests that there is a maximum in plasma pressure for which a magnetic field can provide sufficient magnetic force to balance the pressure gradient force. Therefore, to address the possibility of a pressure balance inconsistency, it is crucial to investigate whether the pressure at the Earth's plasma sheet can increase to this pressure limit.

[51] An unrealistic pressure at the inner plasma sheet can be predicted by a model or simulation if diamagnetic drift, self-consistent magnetic field, or particle distributions are not appropriately taken into account. The pressure increase ratios calculated by *Erickson and Wolf* [1980] are for a drift path from $X = -60$ to -10 R_E along the midnight meridian. However, this drift path can only be possible for low energy particles since their diamagnetic drift is very small. As we discussed in section 4.2, even though the predicted pressure increase ratios are so large (at least a factor of 10 in the study of *Erickson and Wolf* [1980, Figure 3]) it cannot raise the pressure to the magnitude of observed plasma sheet pressure since the pressure borne by low energy protons is so low. These high ratios do not apply to high energy protons, since their drift paths are very different from low energy protons as discussed in section 4.2 and shown in Figure 13.

[52] As discussed in sections 3.1 and 3.4, the magnitude of pressure and of the pressure increase from quiet to moderate activity from our simulation are reasonable as compared with observations, and our magnetic field is able to provide a force-balanced environment. Our magnetic field radial profiles indicates that increased pressure does indeed drive the magnetic field configuration toward its limitation, but the magnetic field configurations we obtain are still far away from forming a neutral point. Therefore, our simulation suggests that the inner plasma sheet under enhanced convection will not face force balance inconsistency at least to a convection strength corresponding to moderate activity. Our steady state solution qualitatively agrees with the solutions by *Hau* [1991], though they obtained field line configurations that are more stretched than those we have obtained. Moreover, our solution is obtained by a simulation with magnetic drift accurately included and the steady state is reached under a dynamic evolution. The conclusion for the force balance inconsistency cannot be drawn conclusively for the plasma sheet for high activity since our current simulation underestimates the pressure for high activity by about a factor of 2. Also, we cannot yet rule out the possibility that an earthward motion of the shielding layer or an increased penetrating electric field could affect the pressure balance.

4.4. Effect of Diamagnetic Drift on Plasma Pressure Increase

[53] We now discuss the roles of diamagnetic drift and the self-consistent magnetic field on the plasma pressure increase in the inner plasma sheet. An increasing convection electric field drives protons closer to the Earth to stronger magnetic field, and thus to smaller flux tube volumes. But the plasma responds by decreasing the magnetic field strength at the inner plasma sheet and by strengthening

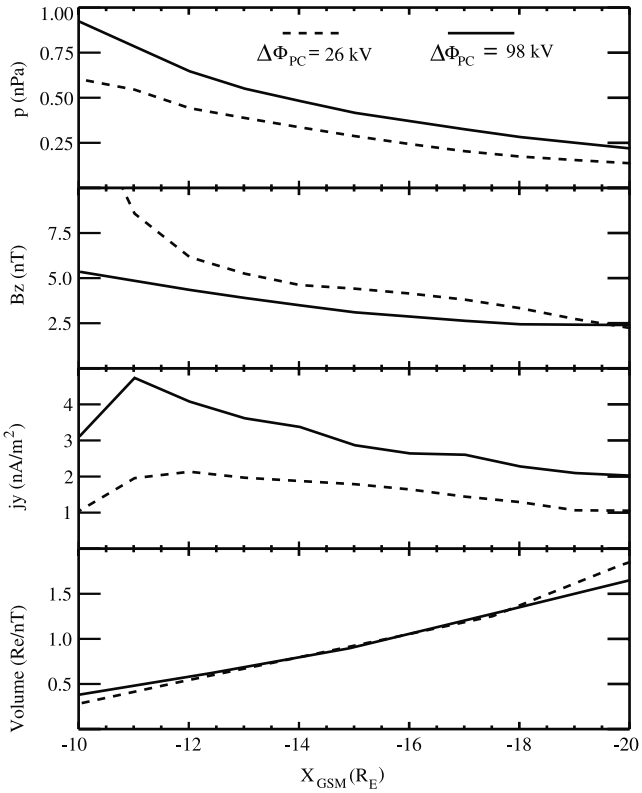

Figure 15. (a) Equatorial proton pressure (nPa), (b) equatorial magnetic field strength (nT), (c) equatorial current density (nA/m^2), and (d) flux tube volume per unit flux (R_E/nT) along the midnight meridian from the modified MSM for $\Delta\Phi_{PC}$ = 26 kV (dashed lines) and for $\Delta\Phi_{PC}$ = 98 kV (solid lines).

the azimuthal current from diamagnetic drift. Furthermore, the increased diamagnetic drift diverts protons around the near-Earth region, reducing the variation in flux tube volume along a drift path and thus moderating the change in pressure and density. We have shown in Figure 13 that the transport of pressure bearing protons in the plasma sheet is strongly affected by diamagnetic drift, and we have also shown in section 3.5 that the diamagnetic drift increases with increasing activity. Therefore, the plasma pressure increase resulting from an increasing convection electric field is restrained by the feedback from the increasing diamagnetic drift.

4.5. Effect of a Self-Consistent Magnetic Field on the Pressure Increase

[54] Figure 15 shows the equatorial proton pressure, magnetic field strength, current density, and magnetic flux tube volume per unit flux as a function of radial distance along the midnight plane for $\Delta\Phi_{PC}$ = 26 and 98 kV. We can see from Figure 2 that the proton pressure increase from $\Delta\Phi_{PC}$ = 26 to 98 kV is larger at smaller radial distances than at larger distances. From force balance, this implies that the lobe magnetic pressure also increases more at smaller radial distances and thus so does the equatorial current per unit distance down the tail. Because of this nonuniform increase in current density as $\Delta\Phi_{PC}$ increases, B_z decreases more from its quiet time value at smaller radial distance than at larger distance, resulting in a flatter radial B_z profile at higher activity as seen in Figure 10. B_z at $X_{GSM} \sim 20\ R_E$ is even slightly higher for $\Delta\Phi_{PC}$ = 98 kV than for $\Delta\Phi_{PC}$ = 26 kV even though current density increases at all radial distances. This is because the negative ΔB generated by the increase of current density at $X_{GSM} < -20\ R_E$ is slightly smaller than the positive ΔB generated by the increase of the current density at $X_{GSM} > -20\ R_E$. Therefore, the net ΔB is positive. The same explanation applies to the increase of magnetic field at larger radial distances for $\Delta\Phi_{PC} >$ 110 kV seen in Figure 10 and the formation of a local field minimum when the current density increases.

[55] The nonuniform increase in the current density causes the flux tube volume to decrease more slowly with decreasing distance from the Earth at higher $\Delta\Phi_{PC}$ as shown in Figure 15. The slopes of the radial profiles of flux tube volume become flatter, implying reduced compression of the plasma as it moves earthward; therefore the feedback of a force-balanced magnetic field to pressure increase is to restrain the pressure increase. Therefore the increased diamagnetic drift and the changes in magnetic field, which are direct consequences of the plasma pressure increase, limit the increase in plasma pressure in the near-Earth plasma sheet and are crucial for maintaining force balance as $\Delta\Phi_{PC}$ is increased.

4.6. Hall Term in the Generalized Ohm's Law

[56] The generalized Ohm's law is

$$\mathbf{E} = -\mathbf{v}\times\mathbf{B} + \frac{1}{ne}\mathbf{j}\times\mathbf{B} + \eta\mathbf{j} - \frac{1}{ne}\nabla\cdot\mathbf{p}_e + \frac{m_e}{e^2 n}\cdot\left[\frac{\partial\mathbf{j}}{\partial t} + \nabla\cdot(\mathbf{jv}+\mathbf{vj})\right] \quad (5)$$

where η is resistivity and $\mathbf{p}_e$ is the electron pressure tensor [*Siscoe*, 1983]. We have used the results from our quiet time simulation to show the Hall term, $\mathbf{j}\times\mathbf{B}/ne$, is not small enough to be neglected within the quiet time inner plasma sheet [*Wang et al.*, 2001]. During enhanced convection, the current density at the equatorial plane increases while the magnetic field decreases due to field line stretching. The number density in our simulation increases with $\Delta\Phi_{PC}$. Therefore, it is important to check if the magnitude of the Hall term is still comparable to the increased convection electric field when $\Delta\Phi_{PC}$ is increased. Figure 16 shows the ratios of the magnitude of the convection electric field **E** to the magnitude of $\mathbf{j}\times\mathbf{B}/(ne)$ using the values obtained from this simulation for $\Delta\Phi_{PC}$ = 98 kV. It is clear from Figure 16 that, despite the decrease of B and increase of n with increasing activity in our simulations, the ratios are less than 2 throughout most part of the inner equatorial plasma sheet. Therefore, the Hall term is still very important as compared to **E** and the frozen-in condition $\mathbf{E} = -\mathbf{v}\times\mathbf{B}$ is still not valid in the inner plasma sheet for moderate activity.

[57] Note that the ratio of $|\mathbf{E}|$ to $|\mathbf{j}\times\mathbf{B}/(ne)|$ is equivalent to the ratio of the magnitude of electric drift to the magnitude of the diamagnetic drift in (4) when $\mathbf{j}\times\mathbf{B} = \nabla p$. Therefore, the region where diamagnetic drift is important is the region where the frozen-in condition is not valid. We have pointed out in section 3.5 the importance of diamagnetic drift in the total drift in the inner plasma sheet, and the good agreement between our simulated total drift and observations supports

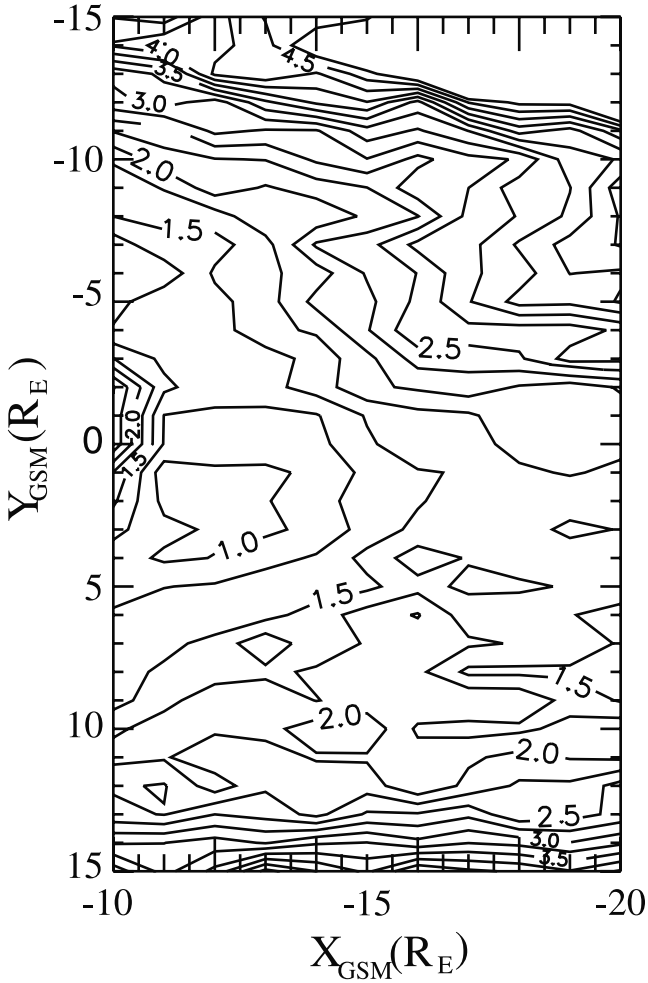

Figure 16. The ratio of the magnitude of the convection electric field ($|\mathbf{E}|$) to the magnitude of the Hall term ($|\mathbf{j} \times \mathbf{B}/(ne)|$) in the equatorial plane for $\Delta\Phi_{PC}$ = 98 kV from the modified MSM.

our conclusion that the Hall term is important in the plasma sheet. The validity of the frozen-in condition in the plasma sheet for high activity will be examined after we are able to accurately simulate the pressure increase observed for high activity.

5. Summary

[58] We have simulated the evolution of protons and magnetic field in the inner plasma sheet from quiet times to moderate and high activity by applying a $\Delta\Phi_{PC}$ that is increased steadily from 26 to 146 kV in 5 hours. The simulation is also run to steady states separately after $\Delta\Phi_{PC}$ is increased to 98 and 146 kV by keeping $\Delta\Phi_{PC}$ constant after it reaches those values. The protons in the plasma sheet are supplied by time-independent boundary particle sources and their electric and magnetic drifts are calculated in a self-consistent magnetic field. The dawnside tail boundary particle sources consist of protons originating from the mantle and LLBL and are based on observations and the finite tail convection model. The duskside tail boundary particle distributions are identical to the dawnside boundary particles distributions without the LLBL contribution. The T96 magnetic field model is supplemented by additional adjustable small-scale current loops that are adjusted self-consistently to maintain 2-D force balance with proton pressure along the midnight meridian. The magnitude of the simulated pressure and temperature in the inner plasma sheet and their increase ratios from quiet to moderate activity are consistent with observations. The simulated number density increases with activity but the dependence is weak. While some observations show increased density with increased activity and some do not, all observations show weak activity dependence for number density. Our simulation underestimates pressure and temperature for high activity by a factor of ~2. This could be a result of some energization processes, such as compression by the solar wind dynamic pressure, not being taken into account in our current simulation. Also, the underestimate might be improved if the temperature (number density) of the boundary particle distribution were allowed to increase (decrease) with activity, as we expect to occur. The change of large-scale features in the 2-D equatorial distributions of plasma bulk parameters from quiet to high activity agree qualitatively with the DMSP observations [*Wing and Newell*, 1998], which indicates that slow drift remains the major contributor to plasma evolution in the inner plasma sheet during disturbed times. The simulated electric drift and diamagnetic drifts both enhance with activity, which keeps the drift direction unchanged. The radial profile of the equatorial magnetic field strength becomes flatter as a result of field line stretching, consistent with the conclusions from observational studies for SMC events. Formation of a local magnetic field minimum at the inner edge of the plasma sheet at high activity is also consistent with other models. However, the minima we have found are quite weak. The plasma pressure is found to keep increasing slowly after $\Delta\Phi_{PC}$ becomes constant at 98 and 146 kV but the increase gradually reaches a steady state, and the total change in pressure and magnetic field after $\Delta\Phi_{PC}$ becomes constant is not large. Thus, the results we have obtained by gradually increasing $\Delta\Phi_{PC}$ are close to steady state results.

[59] The differences in flux tube volume compression along drift paths for low and high energy protons are important to the plasma sheet thermodynamics. The increase ratios for energy and number density due to compression are significantly larger for low energy particles than for high energy particles. This restrains the pressure increase since it is the high energy protons, not low energy protons, that carry most of the pressure.

[60] The diamagnetic drift and self-consistent magnetic field are strongly affected by changes in the plasma pressure within the plasma sheet. We have investigated their responses to the pressure increase when convection is enhanced, and found that their feedbacks significantly restrain the pressure increase. These feedbacks allow for a steady state plasma and magnetic field configuration within the inner plasma sheet in response to enhanced convection. The feedbacks thus prevent the force balance inconsistency in the inner plasma sheet that can result if the diamagnetic drift, the self-consistent magnetic field, or particle distributions are not appropriately taken into account.

[61] A scale analysis based on our results shows that the Hall term in the generalized Ohm's law is not small enough

to be neglected in the inner plasma sheet during convection corresponding to both quiet and moderate activity. Therefore our results suggest that it is not appropriate to use the frozen-in condition, $\mathbf{E} = -\mathbf{v} \times \mathbf{B}$, to approximate the generalized Ohm's law in the region of the inner plasma sheet.

[62] In this study, we used a simplified model for a convection increase and have neglected the variation of boundary conditions with activity and the inward motion of the inner edge of the plasma sheet during enhanced convection. Compression due to enhancements in the solar wind dynamic pressure has also not been considered. This has enabled us to single out the increased convection electric field and investigate its role on plasma transport and energization and magnetic field evolution. The results will also provide a base for comparison when these other factors are taken into account in our future simulations. It also should be remembered that we have only considered force balance along the midnight meridian. We hope to eventually be able to evaluate the affect of 3-D force balance, but this is currently beyond the capabilities of our model.

[63] **Acknowledgments.** We would like to thank N. A. Tsyganenko for his assistance in making modifications to the Tsyganenko 96 magnetic field model. This work has been supported at UCLA by NSF grant ATM-981698. The work by M. W. Chen has been supported by NSF grant ATM-990987 and the Aerospace Technical Investment Program. The work by R. A. Wolf and F. R. Toffoletto has been supported by the NASA Sun–Earth Connection Theory Program under grant NAG5-8131.

[64] Arthur Richmond thanks Wolfgang Baumjohann and another reviewer for their assistance in evaluating this manuscript.

References

Angelopoulos, V., The role of impulsive particle acceleration in magnetotail circulation, in *Proceedings of the Third International Conference on Substorms (ICS-3), Eur. Space Agency Spec. Publ. 389*, pp. 17–22, Eur. Space Agency, Noordwijk, Netherlands, 1996.

Angelopoulos, V., et al., Characteristics of ion flow in the quiet state of the inner plasma sheet, *Geophys. Res. Lett.*, *20*, 1711–1714, 1993.

Angelopoulos, V., et al., Multi-point analysis of a BBF event on April 11, 1985, *J. Geophys. Res.*, *101*, 4966–4990, 1996.

Ashour-Abdalla, M., L. Zelenyi, V. Peroomian, and R. L. Richard, Consequences of magnetotail ion dynamics, *J. Geophys. Res.*, *99*, 14,891–14,916, 1994.

Baumjohann, W., G. Paschmann, and G. A. Cattell, Average plasma properties in the central plasma sheet, *J. Geophys. Res.*, *94*, 6597–6606, 1989.

Baumjohann, W., G. Paschmann, and H. Lühr, Pressure balance between lobe and plasma sheet, *Geophys. Res. Lett.*, *17*, 45–48, 1990.

Borovsky, J. E., M. F. Thomsen, and R. C. Elphic, The driving of the plasma sheet by the solar wind, *J. Geophys. Res.*, *103*, 17,617–17,639, 1998.

Boyle, C. B., P. H. Reiff, and M. R. Hairston, Empirical polar cap potentials, *J. Geophys. Res.*, *102*, 111–125, 1997.

Chen, M. W., M. Schulz, and L. R. Lyons, Energy content of stormtime phase space mapping simulations, *J. Geophys. Res.*, *99*, 5745–5759, 1994.

Erickson, G. M., A quasi-static magnetospheric convection model in two dimensions, *J. Geophys. Res.*, *97*, 6505–6522, 1992.

Erickson, G. M., and R. A. Wolf, Is steady convection possible in the Earth's magnetotail, *Geophys. Res. Lett.*, *7*, 897–900, 1980.

Fairfield, D. H., A. Otto, T. Mukai, S. Kokubun, R. P. Lepping, J. T. Steinberg, A. J. Lazarus, and T. Yamamoto, Geotail observations of the Kelvin–Helmholtz instability at the equatorial magnetotail boundary for parallel northward fields, *J. Geophys. Res.*, *105*, 21,159–21,173, 2000.

Freeman, J. W., R. A. Wolf, R. W. Spiro, and B. Hausman, B. Bales, R. Hilmer, A. Nagai, and R. Lambour, Magnetospheric specification model development code documentation, scientific description, and software documentation, contract F19628-90-K-0012, Rice Univ. for Air Force Geophys. Lab., Hanscom AFB, Mass., July 1993.

Fujimoto, M., T. Terasawa, and T. Mukai, The low-latitude boundary layer in the tail-franks, in *New Perspectives on the Earth's Magnetotail, Geophys. Monogr. Ser.*, vol. 105, edited by A. Nishida, D. N. Baker, and S. W. H. Cowley, pp. 33–44, AGU, Washington, D. C., 1998.

Hau, L.-N., Effects of steady state adiabatic convection on the configuration of the near-Earth plasma sheet, 2, *J. Geophys. Res.*, *96*, 5591–5596, 1991.

Hau, L.-N., R. A. Wolf, G.-H. Voigt, and C. C. Wu, Steady state magnetic field configurations for the Earth's magnetotail, *J. Geophys. Res.*, *94*, 1303–1316, 1989.

Heppner, J. P., and N. C. Maynard, Empirical high-latitude electric field models, *J. Geophys. Res.*, *92*, 4467–4489, 1987.

Hesse, M., and J. Birn, Three dimensional magnetotail equilibria by numerical relaxation techniques, *J. Geophys. Res.*, *98*, 3973–3982, 1993.

Hori, T., K. Maezawa, Y. Saito, and T. Mukai, Average profile of ion flow and convection electric field in the near-Earth plasma sheet, *Geophys. Res. Lett.*, *27*, 1623–1626, 2000.

Huang, C. Y., and L. A. Frank, A statistical survey of the central plasma sheet: Implications for substorm models, *Geophys. Res. Lett.*, *13*, 652–655, 1986.

Huang, C. Y., and L. A. Frank, A statistical survey of the central plasma sheet, *J. Geophys. Res.*, *99*, 83–95, 1994.

Huang, C. Y., C. K. Goertz, and L. A. Frank, Observational determination of the adiabatic index in the quiet time plasma sheet, *Geophys. Res. Lett.*, *16*, 563–566, 1989.

Kivelson, M. G., and H. E. Spence, On the possibility of quasi-static convection in the quiet magnetotail, *Geophys. Res. Lett.*, *15*, 1541–1544, 1988.

Kozyra, J. U., J. E. Borovsky, M. W. Chen, M.-C. Fok, and V. K. Jordanova, Plasma sheet preconditioning, enhanced convection and ring current development, in *Substorms-4*, edited by S. Kokubun and Y. Kamide, pp. 755–760, Kluwer Acad., Norwell, Mass., 1998.

Lannartsson, W., A scenario for solar wind penetration of Earth's magnetic tail based on ion composition data from the ISEE 1 spacecraft, *J. Geophys. Res.*, *97*, 19,221–19,238, 1992.

Miura, A., Kelvin–Helmholtz instability at the magnetopause: Computer simulations, in *Physics of the Magnetopause, Geophys. Monogr. Ser.*, vol. 90, edited by P. Song, B. U. O. Sonnerup, and M. F. Thomsen, pp. 285–291, AGU, Washington, D. C., 1995.

Mitchell, D. G., F. Kutchko, D. J. Williams, T. E. Eastman, L. A. Frank, and C. T. Russell, An extended study of the low-latitude boundary layer on the dawn and dusk flanks of the magnetosphere, *J. Geophys. Res.*, *92*, 7394–7404, 1987.

Nakamura, M., G. Paschmann, W. Baumjohann, and N. Sckopke, Ions distributions and flows near the neutral sheet, *J. Geophys. Res.*, *96*, 5631–5649, 1991.

Ogino, T., R. J. Walker, and M. Ashour-Abdalla, A global magnetohydrodynamic simulation of the magnetosheath and magnetosphere when the interplanetary magnetic field is northward, *IEEE Trans. Plasma Sci.*, *20*, 817–828, 1992.

Otto, A., and D. H. Fairfield, Kelvin–Helmholtz instability at the magnetotail boundary: MHD simulation and comparison with Geotail observations, *J. Geophys. Res.*, *105*, 21,175–21,190, 2000.

Paterson, W. R., L. A. Frank, S. Kokubun, and T. Yamamoto, Geotail survey of ion flow in the plasma sheet: Observations between 10 and 50 R_E, *J. Geophys. Res.*, *193*, 11,811–11,825, 1998.

Richardson, J. D., J. W. Belcher, A. J. Lazarus, K. I. Paularena, and P. R. Gazis, Statistical properties of the solar wind, in *Proceedings of the Eighth International Solar Wind Conference, Dana Point, Calif., AIP Conf. Proc.*, vol. 382, edited by D. Winterhalter et al., pp. 483–486, Springer-Verlag, New York, 1996.

Samson, J. C., L. R. Lyons, B. Xu, F. Creutzberg, and P. Newell, Proton aurora and substorm intensifications, *Geophys. Res. Lett.*, *19*, 2167–2170, 1992.

Sergeev, V. A., T. I. Pulkkinen, R. J. Pellinen, and N. A. Tsyganenko, Hybrid state of the tail magnetic configuration during steady convection events, *J. Geophys. Res.*, *99*, 23,571–23,582, 1994.

Sergeev, V. A., V. Angelopoulos, J. T. Gosling, C. A. Cattell, and C. T. Russell, Detection of localized, plasma-depleted flux tubes or bubbles in the midtail plasma sheet, *J. Geophys. Res.*, *101*, 10,817–10,826, 1996.

Siscoe, G. L., Solar system magnetohydrodynamics, in *Solar–Terrestrial Physics*, edited by R. L. Carovillano and J. M. Forbes, p. 11, D. Reidel, Norwell, Mass., 1983.

Southwood, D. J., and R. A. Wolf, An assessment of the role of precipitation in magnetospheric convection, *J. Geophys. Res.*, *83*, 5227–5232, 1978.

Spence, H. E., and M. G. Kivelson, Contributions of the low-latitude boundary layer to the finite width magnetotail convection model, *J. Geophys. Res.*, *98*, 15,487–15,496, 1993.

Spence, H. E., M. G. Kivelson, and R. J. Walker, Magnetospheric plasma pressures in the midnight meridian: Observations from 2.5 to 35 R_E, *J. Geophys. Res.*, *94*, 5264–5272, 1989.

Spiro, R. W., R. A. Wolf, and B. G. Fejer, Penetration of high-latitude-electric-field effects to low latitudes during SUNDIAL 1984, *Ann. Geophys.*, *6*, 39–50, 1988.

Stiles, G. S., E. W. Hones Jr., S. J. Bame, and J. R. Asbridge, Plasma sheet pressure anisotropies, *J. Geophys. Res.*, *83*, 3166–3172, 1978.

Shue, J.-H. and Y. Kamide, Effects of solar wind density on the westward electrojet, in *Substorms-4*, edited by S. Kokubun and Y. Kamide, p. 677, Kluwer Acad., Norwell, Mass., 1998.

Toffoletto, F. R., R. W. Spiro, R. A. Wolf, M. Hesse, and J. Birn, Self-consistent modeling of inner magnetospheric convection, in *Proceedings of Third International Conference on Substorms (ICS-3), Eur. Space Agency Spec. Publ. 389*, edited by E. J. Rolfe and B. Kaldeich, pp. 223–230, Eur. Space Agency, Noordwijk, Netherlands, 1996.

Toffoletto, F. R., R. W. Spiro, R. A. Wolf, M. Hesse, and J. Birn, Modeling inner magnetospheric electrodynamics, in *Space Weather, Geophys. Monogr. Ser.*, vol. 125, edited by P. Song and B. Kaldeich, pp. 265–272, AGU, Washington, D. C., 2001.

Tsyganenko, N. A., On the convective mechanism for formation of the plasma sheet in the magnetospheric tail, *Planet. Space Sci.*, *30*, 1007–1012, 1982.

Tsyganenko, N. A., Modeling the Earth's magnetospheric magnetic field confined within a realistic magnetopause, *J. Geophys. Res.*, *100*, 5599–5612, 1995.

Tsyganenko, N. A., Effects of the solar wind conditions on the global magnetospheric configuration as deduced from data-based field models, in *Proceedings of the ICS-3 Conference on Substorms, Eur. Space Agency Spec. Publ. 389*, pp. 181–185, Eur. Space Agency, Noordwijk, Netherlands, 1996.

Tsyganenko, N. A., Data-based models of the global geospace magnetic field: Challenges and prospects of the ISTP Era, in *Geospace Mass and Energy Flow: Results From the International Solar–Terrestrial Physics Program*, edited by J. L. Horwitz, D. L. Gallagher, and W. K. Peterson, pp. 371–382, AGU, Washington, D. C., 1998.

Uvarov, V. M., M. A. Kandibolotskaia, and I. V. Moskvin, Dependence of the parameters of the distribution of large-scale electric field on Kp and AE geomagnetic-disturbance indices, *Geomagn. Aeron.*, *29*, 376–380, 1989.

Walker, R. J., T. Ogino, J. R. Raeder, and M. Ashour-Abdalla, A global magnetohydrodynamic simulation of the magnetosphere when the interplanetary magnetic field is southward: The onset of magnetotail reconnection, *J. Geophys. Res.*, *98*, 17,235–17,249, 1993.

Wang, C.-P., L. R. Lyons, M. W. Chen, and R. A. Wolf, Modeling the quiet time inner plasma sheet protons, *J. Geophys. Res.*, *106*, 6161–6178, 2001.

Wang, C.-P., L. R. Lyons, M. W. Chen, and R. A. Wolf, Two-dimensional quiet time equilibrium for the inner plasma sheet protons and magnetic field, *Geophys. Res. Lett.*, *29*(24), 2186, doi:10.1029/2001GL013984, 2002.

Wing, S., and P. T. Newell, Central plasma sheet ion properties as inferred from ionospheric observations, *J. Geophys. Res.*, *103*, 6785–6800, 1998.

Wing, S., and P. T. Newell, 2D plasma sheet ion density and temperature profiles for northward and southward IMF, *Geophys. Res. Lett.*, *29*, 10.1029/2001GL013950, 2002.

Wolf, R. A., The quasi-static (slow-flow) region of the magnetosphere, in *Solar Terrestrial Physics*, edited by R. L. Carovillano and J. M. Forbes, pp. 303–368, D. Reidel, Norwell, Mass., 1983.

Zesta, E., H. J. Singer, D. Lummerzheim, C. T. Russell, L. R. Lyons, and M. J. Brittnacher, The effect of the January 10, 1997 pressure pulse on the magnetosphere–ionosphere current systemin *Magnetospheric Current Systems*, edited by S. Ohtani and R. L. Lysak, p. 217, AGU, Washington, D. C., 2000.

Zhu, X., Magnetospheric convection pattern and its implications, *J. Geophys. Res.*, *98*, 21,291–21,296, 1993.

M. W. Chen, Space Science Applications Laboratory, The Aerospace Corporation, El Segundo, CA, USA.

L. R. Lyons and C.-P. Wang, Department of Atmospheric Sciences, University of California, Los Angeles, CA, USA. (cat@atmos.ucla.edu)

F. R. Toffoletto and R. A. Wolf, Department of Physics and Astronomy, Rice University, Houston, TX, USA.